MICHIGAN STATE UNIVERSITY

CYCLOTRON LABORATORY

PRODUCTION OF NEUTRON-UNBOUND STATES IN INTERMEDIATE-MASS FRAGMENTS FROM ^{14}N + Ag REACTIONS AT E/A = 35 MeV

L. HEILBRONN, A. GALONSKY, C.K. GELBKE,
W.G. LYNCH, T. MURAKAMI, D. SACKETT,
H. SCHELIN, M.B. TSANG, F. DEÁK, A. KISS,
Z. SERES, J. KASAGI, and B.A. REMINGTON

NOVEMBER 1990

MSUCL-749

MSUCL-749
November, 1990

Production of Neutron-Unbound States in Intermediate-Mass Fragments from ^{14}N + Ag Reactions at E/A = 35 MeV

L. Heilbronn, A. Galonsky, C. K. Gelbke, W. G. Lynch, T. Murakami*, D. Sackett, H. Schelin†, and M. B. Tsang

National Superconducting Cyclotron Laboratory

and Department of Physics and Astronomy,

Michigan State University, East Lansing, Michigan 48824

F. Deák and A. Kiss,

Department of Atomic Physics, Eötvös University,

Puskin utca 5-7, H-1088 Budapest, Hungary

Z. Seres

Central Research Institute for Physics,

H-1525 Budapest 114, Hungary

J. Kasagi

Tokyo Institute of Technology,

0-Okayama, Meguro-ku, Tokyo 152, Japan

and

B.A. Remington

Lawrence Livermore National Laboratory,

Livermore, California 94550

Abstract

The populations of neutron-unbound states and of bound states in intermediate-mass fragments have been measured at 15°, 31°, and 64° from the ^{14}N + Ag reaction at E/A = 35 MeV. We did this for eleven neutron-unbound states in seven isotopes whose bound-state populations we were also able to measure. The data are identified in terms of the reaction mechanism producing them, which is either a deep-inelastic mechanism or a quasielastic mechanism. In order to test the assumption that the deep-inelastic data are produced from a thermal source, the unbound-state/bound-state population ratios of deep-inelastic fragments are compared to the predictions of a thermal sequential decay model. Most, but not all, of the deep-inelastic population ratios are fitted with model calculations that assume a source temperature between 2.5 and 3.5 MeV. In the case of ^{13}C we were able to measure four deep-inelastic populations, and in the case of ^{12}B we were able to measure three such populations. To further test the assumption of emission from a thermal source, attempts were made to fit all of the populations from each of these two isotopes with the sequential decay model using a single temperature. The deep-inelastic populations of ^{13}C were fitted with a single temperature between 2.5 and 5.0 MeV. The deep-inelastic populations of ^{12}B were not fitted with any temperature. There is enough of the deep-inelastic data that is not fitted with the predictions of a thermal model that the assumption of a thermal source for the production of deep-inelastic fragments may be incorrect, or there may be other effects present which alter the thermal properties of the data. The quasielastic populations in each ^{12}B and ^{13}C were also measured and could not be fitted with the model using a single temperature, which is consistent with the assumption of a nonthermal source of production for quasielastic fragments. The dependence of the unbound-state/bound-state population ratio on the fragment kinetic energy shows a difference between the quasielastic and deep-inelastic data. For quasielastic fragments whose mass is near the mass of the beam, the ratio decreases towards zero as the fragment velocity approaches the beam velocity. In contrast, the ratio for half-beam mass quasielastic fragments is constant or only slightly decreasing as the kinetic energy increases. The ratio for deep-inelastic fragments is approximately constant as a function of kinetic energy, independent of fragment mass. The amount of feeding from several neutron-unbound channels into bound states is measured and compared to the sequential

decay model. The model successfully predicts the amount of feeding from most of the channels using a source temperature of 2.5 to 4.0 MeV. The effect of feeding on both spectral temperatures and on population temperatures is investigated. We conclude that the effect of feeding on both temperatures, as determined by model calculations, cannot account for the discrepancy in the values between the two.

I. Introduction

An important property of intermediate energy (E/A ≈ 20-200 MeV) heavy-ion reactions is the production of intermediate-mass fragments (for this paper, $3 \leq Z \leq 7$, $6 \leq A \leq 14$, referred to as IMFs). Both IMF and light particle spectra yield information about the reaction mechanisms governing their production, but IMFs bear additional information not found with very light particles, such as neutrons and protons. Specifically, IMFs are produced in excited states, and measurements of the populations of those states can be readily applied to an understanding of IMF production. In this paper we report on the populations of several neutron-unbound states of IMFs and their relevance to models used to explain IMF production.

In general, systems that have no fissionable products appear to produce IMFs from two different types of reaction mechanisms. Quasielastic (QE) processes dominate IMF spectra at high IMF kinetic energy at or near the grazing angle. Deep-inelastic (DI) processes dominate IMF spectra for all IMF kinetic energies at angles much greater than the grazing angle and for low IMF kinetic energies at or near the grazing angle. The main difference between QE and DI processes is that DI fragments seem to come from a thermal source, whereas QE fragments appear to come from a nonthermal source.

Quasielastic IMF inclusive spectra have been detected in several systems.[1-9] The fragmentation models of Goldhaber[10] and Friedman,[11] which are successful in describing IMF spectra in high-energy heavy-ion collisions, are moderately successful in describing IMF spectra in intermediate-energy collisions. Nucleon-exchange models, such as the stripping-pickup model,[12] have been more successful in describing the general features of intermediate-energy IMF spectra.

Populations of excited states of QE-produced IMFs, especially the populations of excited-state IMFs with large kinetic energies,[12,13] should bear information on the partition of excitation energy between reaction partners.[13] The dependence of excited IMF population on IMF kinetic energy is seen as an important test of nucleon-exchange models[13-15] used to describe QE IMF production. It is interesting to note that two reports[12,13] on the dependence of IMF excitation as a function of kinetic energy are quite different from each other. As the kinetic energy increases, the excitation of

particle-bound IMFs is roughly constant,[13] but in contrast the excitation of the neutron-unbound 3.388-MeV state in ^{12}B falls off rapidly to zero near the velocity of the beam.[12]

Deep-inelastic IMF spectra have been parameterized for a wide range of systems[16-21] using the moving-source model.[22] In general, most of the IMFs come from a source with a velocity roughly one-third of the beam velocity.[9,19] As the beam energy increases, the source temperature also increases, which is consistent with the assumption of creating a thermal source. For the system used in this paper (E/A = 35 MeV, ^{14}N + Ag), the source temperature extracted from IMF spectra is about 13 MeV.[9,19]

Both particle-bound excited states[23-27] and particle-unbound states[12,16,17,20,21,25,28-37] in IMFs have been detected in several systems. The measured populations of these states can be used to calculate temperatures from a Boltzmann population distribution. The population ratio of two states of the same nucleus is related to the population temperature (T) in the following way:

$$R = \frac{2J_1+1}{2J_2+1} \exp(-\Delta E/T) \qquad (1)$$

where R is the ratio of the population of state 1 to the population of state 2, J_1 and J_2 are the state spins, and ΔE is the difference in level energy between state 1 and state 2. If it is assumed that excited, DI IMFs come from a thermal source, then the population ratio gives the temperature of that source, just as IMF kinetic energy spectra give that temperature. For the system investigated in this paper, the temperatures that have been deduced from excited state populations have ranged from ~0.6 MeV to ~3 MeV. These population temperatures are much lower than the corresponding spectral temperatures. Large discrepancies between population temperatures and spectral temperatures have also been reported for other systems.[17,21,27]

One possible explanation for the discrepancy between a population temperature and a spectral temperature measured for the same system is that sequential feeding from higher lying states may alter the measured populations of ground and excited states from their initial populations, making this

experimentally derived "apparent" population temperature different from the "true", or initial, source temperature.[29,38] The initial temperatures derived from analyses that compensate the measured state populations for feeding range from ~2.5 MeV to 5 MeV.[27,31,20] Thus, after taking feeding into account the extracted population temperatures are still much lower than the spectral temperatures. To date, no attempt has been made to determine the effect feeding has on spectral temperatures deduced from IMF spectra.

Another method that can be used to test the assumption that unbound IMFs are produced by thermal sources is to plot the dependence of R (Eq. 1) on the fragment's kinetic energy. For example, if DI-unbound IMFs were emitted from a source that behaved as a thermal source of infinite extent, one would expect the population ratio (R) to be constant as a function of IMF kinetic energy. Other thermal models may predict a different behavior of R on kinetic energy, thus the data on R versus kinetic energy can be sensitive to the details of the thermal model used to describe the production of unbound IMFs.

There is some data that suggests that DI excited-IMFs are not produced by a thermal source. One group has measured the populations of seven states in the same isotope and has reported that it is not possible to fit a single temperature to all seven populations, even after taking feeding into account.[36] Also, the finding of population temperatures that are constant as a function of beam energy (from E/A = 11 MeV to E/A = 94 MeV)[16,20,26,27,35,39,40] is inconsistent with the assumption of emission from a thermal source, as one would expect the temperature to rise as more energy is dumped into the system. However, the fact that a single source temperature is found for a large range of isotopes and states created in the same system is consistent with the assumption of a thermal source.[20,27] So the question of the validity of assumed thermal sources is still open.

In this paper we report on the populations of several IMF neutron-unbound states produced in the E/A = 35 MeV, ^{14}N + Ag system, for both QE and DI IMFs. This work expands on the data previously reported on neutron-unbound states produced from this system.[12,25] The assumption of thermal production of DI IMFs will be tested by attempting to fit temperatures extracted from state populations to a single, initial source temperature with the aid of a sequential feeding calculation. The dependence of R (Eq. 1) on IMF kinetic energy for both QE and DI IMFs will also be reported. Predictions of the

feeding from the model calculation will be compared to data on the feeding from several neutron-unbound channels. The effect of sequential feeding on both population temperatures and spectral temperatures will be investigated in an effort to resolve the discrepancy between the two temperatures.

II. Experimental Method

We measured neutron-fragment coincidences produced by collisions of ^{14}N projectiles at 35 MeV/nucleon with a Ag target. Since one of the goals of the experiment was to measure the populations of neutron-unbound states created during these collisions, and since there is a strong kinematical focussing of the neutrons that come from the decay of these states,[41] the neutron and fragment detectors were set up in a colinear alignment. Three such setups were placed at 15°, 31°, and 64°.

The neutron detectors we used were glass cells filled with liquid scintillator. Two types of scintillator were used, NE-213 and BC-501, with no discernable differences in performance detected between them during data taking and analysis. Each cell was a cylinder approximately 7.6 cm long and 12.7 cm in diameter. The back of each cell had a conical plastic (lucite) light pipe glued to it, which in turn had a 5.1 cm diameter photomultiplier tube glued to it. Each detector was housed in a thin aluminum can 15.25 cm in diameter, with a small amount of foam padding between the glass cell and the can. The intrinsic timing resolution of these detectors, when measured using γ rays from a ^{60}Co source, was 0.9 ns on the average.

A close-packed array of three neutron detectors was centered at 15°, with a distance of 457 cm from the target to the centers of the scintillator cells. The array subtended a half angle of 1.9°, with 50% of the available solid angle in that space taken up by scintillator. Two close-packed arrays of seven detectors each were centered at 31° and 64°, with distances from target to cell centers of 438 cm and 354 cm, respectively. The array at 31° subtended a half angle of 2.8°, and the array at 64° subtended a half angle of 3.5°. Both arrays had 58% of the available solid angle taken up by scintillator.

Fragment isotope identification and energy determination were achieved using solid-state Si detectors. Two-element, ΔE-E telescopes were used at 31° (94μ and 5mm) and 64° (74μ and 5mm). At 15°, where some Li fragments have a large range, a four element, ΔE-ΔE-E-E telescope (94μ, 97μ, 5mm, and 1mm) was used. Every element was cooled to -10°C. Good isotope identification and

good separation of IMFs were achieved using these telescopes. Fragment energy calibration was done with alpha particles from a ^{228}Th source, using a calibrated pulser to extend the calibration to higher energies. Fragment energies were determined with an uncertaintity of ±2%.

A copper collimator with a thin (10 mg/cm^2) gold foil placed on its front face was placed in front of each telescope. The foil was used to attenuate electrons and x rays knocked out from the target. The collimator at 15° subtended a half angle of 1.9° and a solid angle of 3.5 msr. The collimators at 31° and 64° both subtended half angles of 2.9° and solid angles of 8.1 msr.

Neutron energies were determined by using a time-of-flight technique that used neutron and fragment signals as the start and stop, respectively, of a timing circuit. The timing signal from the fragment side of the circuit came from the first ΔE element of each telescope with the aid of a time-pickoff unit. The timing signal from the neutron side came from the fast (anode) pulse from the neutron detector. The overall timing resolution of this system was determined by looking at the prompt Y rays in our time-of-flight spectra, and was 0.9 ns for all three angles, which indicates that the intrinsic timing resolution of each neutron detector was the limiting factor in the overall timing resolution of the detection system.

Silver targets of 5.0 mg/cm^2 and 3.9 mg/cm^2 were rotated 45° with respect to the beam in order to minimize the energy loss of reaction products at 15°, 31°, and 64° in the target. No visible surface contamination of the targets from pump oils or coolant liquid was noted during the experiment.

The K-500 cyclotron at Michigan State University produced a 1 ns burst of beam every 52.4 ns. The energy of the ^{14}N ions, 490 MeV, was known to ±2%. Typical beam intensity used during the experiment was about 1.5×10^{10} particles per second.

In order to measure the number of background neutrons produced during the experiment, shadow bars were placed between the target and neutron detector arrays. Each bar was long enough (50.8 cm at 15°, 40.6 cm at 31°, and 30.0 cm at 64°) to stop more than 99% of the neutron flux coming from the target directly to the neutron detector. About 40% of the beam time was dedicated to measuring background neutrons.

Separate runs were made intermittently during the experiment to measure fragment singles. Bound-state populations were determined from the singles data.

III. Data Analysis

The goal of the data analysis was to measure both bound-state and neutron-unbound-state populations in IMFs. Before the populations were determined it was necessary to apply corrections to both the IMF singles and IMF-neutron coincidence data. Once these corrections were made, IMF singles spectra and IMF-neutron relative velocity spectra were produced, and from these spectra the state populations were extracted.

A. IMF Singles Data

As previously mentioned, IMF energies were determined using calibrated silicon telescopes. Small corrections to these energies were needed to compensate for energy loss in the target and the gold foil that preceded each telescope. In addition, the energy loss in the dead layers of the silicon detectors was also taken into account. After applying the corrections to IMF energy on an event-by-event basis, IMF singles spectra were generated for each isotope at 15°, 31°, and 64°. Shown in Fig. 1 are the singles spectra for selected isotopes at 15° and 31°. The solid, dashed, and dotted lines are from a fitting that will be explained in the results section. The combined population of ground state and all bound states of a particular IMF was determined from the IMF's singles spectrum.

B. IMF-Neutron Coincidence Data

The corrections which were applied to the IMF kinetic energy are also needed for a precise determination of the neutron energy, since neutron energies were determined from a time-of-flight method that used the fragment signal for the stop, requiring us to add the fragment flight time to the neutron-fragment time of flight. Neutron/Y-ray separation was achieved with two-dimensional pulse shape discrimination.[42]

Once the neutron flight time was determined for each event, corrections were made for the neutron side of the event. The energy dependent neutron detection efficiency for each detector was calculated using the code TOTEFF,[43] and these calculations were compared to the efficiencies computed using a Monte-Carlo code developed by Cecil et al.[44] The results from the two codes disagreed by at most 10%, and this value was taken as the uncertainty in the efficiencies. The loss of neutron flux due to out-scattering from materials between the target and neutron detector (silicon detectors, steel vacuum

chamber wall, air, aluminum neutron detector can, and glass cell) was estimated using a code developed by Remington.[45] Other energy dependent corrections such as the background subtraction and accidentals subtraction were also made. All corrections were applied on an event-by-event basis.

After the corrections were made, relative velocity spectra were constructed for our colinear coincidence events. Figure 2 shows a relative velocity spectrum for neutrons in coincidence with ^{12}C at 15°. The abcissa shows the value of the fragment velocity minus the neutron velocity, while the top of the figure shows the relative energy between the fragment and neutron. Included in Fig. 2 is an energy level diagram which indicates the decays that show a resonance in the corresponding relative velocity plot. The solid line shows a fit to the data from Monte Carlo simulations (described later in this section) of the decays of the numbered resonances into our detection system added onto a background. The background is indicated with the dotted line.

Looking at Fig. 2, one notes that for each decay from a single state or group of states there are two peaks, one at a negative relative velocity and one at a positive relative velocity. These two peaks are a result of the kinematical focussing of the decay neutron and our finite detector geometry. Figure 3 illustrates the decay of an excited fragment into a daughter fragment and a neutron. The dashed lines indicate the available solid angle for neutron and fragment detection. For simplicity, the daughter recoil momentum is neglected and the solid angles of the neutron and fragment detectors are taken to be equal. If the decay energy is large enough, only the most forward-focussed neutrons (which give a negative relative velocity) and the most backward-focussed neutrons (positive relative velocity) will be detected. In this way two peaks are created for each decay. The peak at negative relative velocity will be larger than its companion peak at positive relative velocity since the available solid angle in the decay frame for detection (the geometrical efficiency)[25] is greater for forward-focussed neutrons.

If the decay energy is small enough, all of the neutrons will be focussed into the neutron detector, and as a result there will only be one peak in the corresponding relative velocity spectrum, and it will be centered at 0 cm/ns. Such a case is best shown in Fig. 4, where the central peak is due to the decay of the 3.388-MeV state of ^{12}B to the ground state of ^{11}B. For this decay, the decay energy is only 18 keV, and our geometrical efficiency is about 33% (note that this value of the geometrical efficiency is much greater

than the percentage of the available solid angle in the lab taken up by the neutron detectors, which is about 0.17% - thus the kinematical focussing increases our counting rate by a factor of ~200). Since the efficiency is less than 100%, one might expect the forward and backward peaks to be separated. Although there is a dip in the peak at 0 cm/ns, clearly the forward and backward peaks are unresolved from each other. The reason they are unresolved is due to our instrumental resolution. Hence, only one peak is observed for this decay.

For this experiment, the relative velocity resolution, dv_{rel}, was about 2 mm/ns for all of our spectra. The corresponding relative energy resolution is related to the relative velocity resolution by $dE_{rel}=\mu v_{rel} dv_{rel}$, where μ is the reduced mass of the daughter-fragment/neutron system. Thus, as the decay energy increases, the relative energy resolution gets worse, even though the relative velocity resolution remains the same. Because of this, our ability to resolve individual decays decreases as the decay energy increases. Figure 2 shows the relative energy resolution for two of the decays. For E_{rel}= 0.1 MeV, for example, dE_{rel}= 90 keV, whereas for E_{rel}= 2 MeV, dE_{rel}= 450 keV. The energy resolution at a particular value of relative velocity will vary slightly, of course, depending on the mass of the fragment in question, but not by much.

Since the geometrical efficiency for all our detected decays was less than 100%, it had to be calculated in order for us to extract the total population of the neutron-unbound states detected in our relative velocity spectra. Fragment and neutron detector sizes and flight paths, initial fragment velocity, level decay energies and level widths all have an effect on the geometrical efficiency, and were put into the Monte Carlo code MONTRES,[41] which simulates the decay of neutron-unbound states into our detection system. Conditions which affect the energy determination of the fragments, such as silicon detector resolution and target thickness, and conditions which affect the timing resolution of the neutron detectors, such as detector thickness and intrinsic timing resolution, are also put into the code. The solid lines in Figs. 2 and 4 show the fits to the data using the decay simulations from MONTRES added onto a background. The spectral resolution and spectral shapes are matched well with the simulations. It should be noted here that the decay is assumed to be isotropic in the rest frame of the parent fragment. Data

from another experiment that used the same system as ours has been analyzed to test this assumption on states that decay by emission of charged particles,[46] and no evidence has been found that contradicts an assumed isotropic decay. It should also be noted that for all cases except one, the level widths used in the simulations are taken as constants in Lorentzian resonance functions. The one exception is for the decay of the 7.46-MeV state in ^{7}Li to the ground state of ^{6}Li. Here the reported width, 89 keV,[47] is close enough to the decay energy, 210 keV, to take into account the energy dependence of the width. The energy dependence was calculated using penetrabilities from Ref. 48.

The precise nature of the background in the spectra shown in Figs. 2 and 4 is not known. A background has been calculated using random coincidences between fragments and neutrons and has been used in previous analyses,[25,32] although it cannot account for all the background. It is a broad Gaussian whose peak is, in general, at some nonzero value of relative velocity. The dotted lines in Figs. 2 and 4 show this type of background. In order to estimate the effect the uncertainty in background determination had on the extracted level populations, all the spectra were fitted using at least two types of backgrounds. The background just mentioned was always used, and others that were used are Cauchy backgrounds, Tippet functions, and linear backgrounds. An average population from all backgrounds was calculated, and the deviation from the average was used as the uncertainty in the population due to the background.

In addition to the uncertainty in the population due to the background, statistical uncertainties and systematic errors (such as an assumed detector misalignment, current integrator error, target thickness nonuniformity, etc.) were also included in the final uncertainties reported for our populations, ratios, and temperatures. In most cases, the background uncertainty and statistical error were the main contributors to the final uncertainty.

IV. Results

A. IMF Singles Spectra : Population of Bound States

The solid lines in Fig. 1 indicate fits to the singles spectra using the sum of two functions which are represented by the dotted and dashed lines. The dotted lines show the fits to the deep-inelastic parts of the spectra with the function:

$$F_{DI} = N_{DI}(E/A)\exp(-E\rho) \qquad (2)$$

where N_{DI} and ρ are the fit parameters, A is the mass number, and E is the kinetic energy of the fragment. The dashed lines show the fits to the quasielastic parts with the function:

$$F_{QE} = N_{QE}\sqrt{(E/A)}\exp[a\sqrt{(E/A)}]\{1+\exp[b(E/A-E_o/A)]\}^{-1} \qquad (3)$$

where N_{QE}, a, b, and E_o are the fit parameters. The parameterization of the QE data is the same as the one used in Ref. 8. It allows us to estimate the percentage of QE IMFs and DI IMFs in the bound-state yields at 15° and 31° for various cuts on IMF kinetic energy, which in turn allows us to identify which regions of IMF kinetic energy are dominated either by QE or DI reaction mechanisms. We assume that these regions are the same for unbound-state IMF production as for bound-state IMF production. Table I shows the percentage of QE IMFs in the bound-state yield for various cuts on IMF kinetic energy at 15° and 31°. All of the yield at 64° is assumed to come from DI reactions. No IMF data below a kinetic energy of 6 MeV/nucleon was used in this paper.

The singles spectra for ^{7}Li contain some events from the double alpha breakup of ^{8}Be which appear as ^{7}Li.[49,50] The contamination can be corrected for if the ^{8}Be spectrum is known at the angle of interest and if the efficiency for collecting both alphas from the breakup of ^{8}Be into the detection system is known. We did not measure the ^{8}Be spectra at any of our angles, but the ^{8}Be spectrum at 50° has been measured for the same system as ours[50] (namely ^{14}N + Ag at E/A = 35). As in Ref. 50, we assume that the ^{8}Be spectra at 31° and 64° have the same spectral shape as the ^{9}Be spectra at those angles, and we assume that the ratio of the ^{8}Be yield to the ^{9}Be yield, which is equal to 2.1 at 50°,[50] is also equal to 2.1 at 31° and 64°. Since the data from Ref. 50 is from DI reactions only, we did not use their results at 15°, where there is a strong contribution from QE processes. At 15°, the yield of ^{8}Be at a particular E/A was estimated from the interpolation of the yields of ^{7}Be, ^{9}Be, and ^{10}Be we measured at the same E/A. Once the double-alpha collection efficiency was calculated, the measured ^{7}Li spectrum was corrected for ^{8}Be contamination.

B. IMF + Neutron Coincidence Data : Unbound-State Populations

Unbound-state populations were determined from analyses of relative velocity spectra such as the ones in Figs. 2 and 4. For most of the cases, the level energies, spins, and widths used for the analysis of all the bound-state and unbound-state populations come from Refs. 47, 51, and 52. The branching ratio of the 7.456-MeV state in ^{7}Li (Γ_n/Γ_{tot}= 0.776) was calculated using the reported partial widths at resonance.[47] The energy and width of the 4.296-MeV (Γ = 60 keV) state in ^{9}Li were taken from a separate analysis of this data,[53] and the spin of this state (J = 5/2) comes from Ref. 54. Using the data from Ref. 55, we estimate that the decay of the overlapping 9.27-Mev and 9.4-MeV states of ^{10}Be to the ground state of ^{9}Be accounts for 93 ± 8 % of the combined total width. The branching ratio of the decay of the 9.5-MeV state in ^{13}C to the ground state of ^{12}C is taken to be 0.90.[56] The width (Γ = 210 keV) and energy of the 19.234-MeV state in ^{8}Be were taken from Ref. 53.

1. Two-Level Ratios

If DI IMFs come from a thermal source, the ratio of two populations from the same IMF should be described by a Boltzmann population distribution (Eq. 1). One would expect the DI population ratios for all of the isotopes to reflect the same source temperature, independent of IMF mass, since spectral temperatures derived from IMF singles spectra are independent of IMF mass[9,19]. In this section we determine the ratio of two populations from the same IMF, one of which is the population of a neutron-unbound state (or group of unresolved unbound states) as determined by IMF + neutron relative velocity spectra, and the other of which is the population of the bound states (ground state + all particle-bound states) as determined from IMF singles spectra. We then use these "two-level ratios" along with Eq. 1 to test the thermal nature of the mechanism producing DI IMFs.

In total, eleven unbound-state populations were determined from seven isotopes whose bound-state populations we were also able to determine. For each of these eleven states the ratios of its population to the bound-state population (R of eq.1) is shown in Figs. 5. The data are labeled with the appropriate unbound-state energy. The error bars include all of the uncertainties discussed in the data analysis section. The histograms show predictions for the population ratios from a sequential feeding model that

will be explained later in this section. The lefthand plot in Fig. 5 is for IMFs at 15°, with the open symbols representing the QE data and the solid symbols denoting the DI data. The middle plot of Fig. 5 is for DI IMFs at 31°, and the righthand plot shows the data at 64°.

At 15°, the region of kinetic energy taken to be DI is 6-10 MeV/nucleon except for the 8.3-MeV state in ^{14}C and the 3.756-MeV state in ^{12}B, where the statistical accuracy was good enough only for a cut of 6-15 MeV/nucleon. We were unable to determine the populations of the 4.236-MeV state in ^{9}Li and the 9.27-MeV + 9.4-MeV states in ^{10}Be with any statistical accuracy in the region of DI production. The percentage of QE data from 6 to 10 MeV/nucleon and from 6 to 15 MeV/nucleon for a particular isotope can be seen in Table I. All of the data above 15 MeV/nucleon is at least 87% QE. Again, the percentage of QE data in a particular kinetic energy range was estimated from the analysis of IMF singles spectra using Eqs. 2 and 3.

The DI region at 31° was taken to be all energies above 6 MeV/nucleon, except for the 3.388-MeV and 3.756-MeV states in ^{12}B and the 7.37-MeV + 7.54-MeV group of states in ^{10}Be, where the DI region was taken to be 6-15 MeV/nucleon. The reason for taking a smaller kinetic energy gate was to reduce the amount of contamination from QE processes (see the 31° columns of Table I). Statistics were not good enough to take the smaller gate for the 9.27-MeV + 9.4-MeV group of states in ^{10}Be. All of the data at 64° is DI.

We now address the question of whether or not the DI two-level population ratios appear to be produced from a thermal source. Source temperatures can be readily calculated from the population ratios using Eq. 1, and those temperatures can be compared with each other to see if they all agree. However, the effects of sequential feeding[38] from higher-lying states into unbound-state and bound-state populations will yield an experimentally measured "apparent" temperature different from the "true", or initial, source temperature. Thus, if one is to test whether or not a large number of population ratios from different isotopes are described by a thermal source with a single temperature, the effects of sequential feeding must be taken into account.

The histograms in Figs. 5 and 6 represent the population ratios calculated with the final bound and unbound-state populations predicted by a sequential feeding model. The model we used has been reported on in several papers,[27-29,36] so only the major features will be described here. The

calculation creates a primary, or "initial", population of IMFs in bound and unbound states, with all of the populations characterized by a single temperature. The decay of these fragments is then followed until a ground state fragment is reached. The decay of a fragment from the initial distribution may follow several steps before finally decaying to a ground state fragment. The populations of the "final step" states, i.e., the populations of the levels that decay directly to a bound state of a fragment, are also calculated in the model. Population ratios, such as the ones we measure in the laboratory, are then calculated using the final step unbound-state populations and the final ground state populations predicted by the model.

For this paper the model calculated the feeding from higher-lying states in nuclei with $Z \leq 13$. The model considered both discrete states and continuum states in these nuclei. When known, complete spectroscopic information (level energy, spin, parity, width, branching ratio, isospin) for each level was put in for the discrete states. When unknown, values for the spin, isospin, and parity were selected randomly from a set of most likely values that were determined from the noninteracting shell model developed by B.A. Brown of Michigan State University. Unknown branching ratios were calculated using the Hauser-Feshbach formula.[57] The feeding calculation was repeated for different choices of the randomly selected values to determine the uncertainty in the calculation due to these values.

Looking at Fig. 5, one notes that for each initial source temperature there is a pair of histograms showing the prediction of the measured population ratio. The pair of histograms represents the uncertainty in the calculation by showing the highest and lowest values of the population ratio obtained from the feeding model calculations.

The solid histograms in Figs. 5 show the predictions of the population ratios for an initial source temperature of 2.5 MeV, and the dotted histograms show the predictions for a temperature of 3.5 MeV. It is in this range of initial source temperatures that the model best predicts the measured DI population ratios at 15° and 31°. The dashed line in Fig. 6 for 64° is for a source temperature of 6 MeV.

Looking at the DI population ratios at 15° (solid symbols), we see that seven of the nine ratios are fitted by the model predictions for initial temperatures between 2.5 and 3.5 MeV. Of the two that were not fitted, only one, that being the 2.255-MeV state in ^{8}Li, is more than two standard

deviations away from the model predictions. This may not be surprising since 43% of the inclusive ^{8}Li data in this region comes from QE processes. At 31°, eight of the ten DI population ratios are fitted by the model calculations for source temperatures between 2.5 and 3.5 MeV.

Based on the results for DI ratios at 15° and 31°, it appears that the data is consistent with a thermal model whose source temperature is between 2.5 and 3.5 MeV. However, the data at 64° cannot be fitted by the model predictions, even for a range of 2.5 to 6 MeV. Only one point, the point for the 9.5-MeV state in ^{13}C, agrees with the model predictions with source temperatures between 2.5 and 3.5 MeV. The point for the 7.46-MeV state in ^{7}Li agrees with a source temperature between 3.5 and 6 MeV, but the other three points are outside the range between 2.5 and 6 MeV. Looking at the data and model predictions for the 3.388-MeV state in ^{12}B and the 7.37-MeV + 7.54-MeV states in ^{10}Be at 64°, it appears that no model calculation will agree with the data. As the source temperature increases from 2.5 to 3.5 MeV the predicted ratio also increases, but as the temperature increases to 6 MeV, the predicted ratio decreases to a value below the prediction for 2.5 MeV. This indicates that the model will predict a maximum value of the ratio that will be below the measured ratio in both cases.

It is interesting to note that, for the most part, the measured DI and QE population ratios at 15° (Fig. 5) are similar. The noteable exceptions are the group of states near 7.5 MeV in ^{13}C, the 3.388-MeV state in ^{12}B, and the 7.37-MeV + 7.54-MeV group of states in ^{10}Be. Otherwise, it appears that the population ratios for QE IMFs are almost the same as those for DI IMFs. Thus the amount of contamination from QE processes in a predominantly DI region does not produce a significant error in the determination of R for the DI process, in most cases.

2. Multilevel Populations

Another test which can be applied to the DI population data to see if they are consistent with emission from a thermal source is to check whether three or more populations from the same nucleus can be fitted with a single temperature. Figure 6 shows a plot of the natural logarithm of the population (divided by the appropriate spin factor) of each of the three unbound states and of the bound states detected for ^{13}C at 15° for the indicated cuts on fragment energy. Each point is plotted at its appropriate level energy. All of the bound states were treated as a single state whose level energy is 2.3

MeV, and whose effective spin factor (2J+1) is 12.22. The value of the effective spin factor depends on the temperature, but for temperatures between 2 and 6 MeV it varies only from 11.95 to 12.50. This variance in the spin factor was included in the uncertainty for that data point.

If all four groups of states were populated according to a Boltzmann population distribution, and if the effect of sequential feeding was negligible, then all four points in each plot of Fig. 6 would lie on a straight line. This appears to be the case for E_{frag} between 6 and 10 MeV/nucleon and for E_{frag} between 10 and 15 MeV/nucleon. The solid, dashed, dotted and dot-dashed lines in each plot indicate the predicted populations (relative to the bound-state population) from the sequential feeding model for initial temperatures of 2, 3, 4 and 5 MeV, respectively. Below 10 MeV/nucleon, the data is fitted with the model calculations using initial temperatures of 3, 4, and 5 MeV. The data for 10-15 MeV/nucleon is nearly fitted with the model calculation. According to Table I, 25% of the bound-state yield below 15 MeV/nucleon is quasielastic, while below 10 MeV/nucleon it is 12%. Thus it appears that for the ^{13}C data dominated by DI processes, the measured populations are indicative of a thermal reaction mechanism. Above 15 MeV/nucleon none of the data can be fitted with the model calculation, although the data from 30-40 MeV/nucleon is nearly fitted. This is consistent with the assumption of a nonthermal reaction mechanism for the production of QE IMFs.

Figure 7 shows the plot of the logarithm of three populations in ^{12}B, the 3.76-MeV state, the 3.388-MeV state, and the bound states. The bound states were treated as the bound states of ^{13}C were in Fig. 6. The left plot in Fig. 7 is for 15° and 6-15 MeV/nucleon, the middle plot is for 15° and 15-40 MeV/nucleon, and the right plot is for 31° and 6-15 MeV/nucleon. The solid, dashed, dotted, and dot-dashed lines represent the same temperatures as in Fig. 6. As in Fig. 6, the QE data (middle plot) is not fitted by any of the model predictions. However, none of the DI data is fitted, either, which is in contrast to the results presented in Fig. 6, where the DI data is fitted and the QE data is not.

In regards to the nature of the DI reaction mechanism, the results from the two-level and multilevel data are not clear. Some of the DI data can be fitted with a thermal model, but there are some exceptions which are not fitted. What this data may indicate is that the DI reaction mechanism may

indeed be thermal in nature, but that there are other effects present during the reaction which are not accounted for in the model which can skew some of the measured populations such that they appear to be nonthermal. One such effect could be "final-state interactions,"[58] for example. The data may also indicate that while feeding calculations like the one we used may be generally correct, it may not be correct for every final state.

V. R versus Kinetic Energy

While there are a few cases where the QE population data is clearly different than the DI population data, for the most part no distinction can be made between the two. However, it should be pointed out that up to this point most of the data shown has been for rather large cuts on IMF kinetic energy. The difference between QE and DI data becomes more obvious when the populations are examined with smaller cuts on kinetic energy, particularly when R (Eq. 1) is plotted as a function of the kinetic energy.

The dependence of the ratio of an unbound-state population to the bound-state population on IMF kinetic energy is shown for the 7.456-MeV state in ^{7}Li, the 2.255-MeV state in ^{8}Li, the 3.388-MeV state in ^{12}B, and the 9.5-MeV state and 7.5-MeV group of states in ^{13}C in Figs. 8-11, respectively. The upper plots show R versus kinetic energy, while the lower plots show the corresponding singles spectra. In Fig. 8, the filled points show the data after correcting the inclusive spectra for ^{8}Be contamination, and the open symbols show the data before the correction. The top plot in Fig. 11 is for the group of three states near 7.5-MeV in ^{13}C, and the middle plot is for the 9.5-MeV state. For reference, a temperature scale computed from Eq. 1 without corrections for feeding is included in the upper plots of Figs. 8-11. The numbers in the upper plots indicate the percentage of QE data in the bound-state yield at a particular energy gate.

A. QE IMFs

The dependence of R on IMF kinetic energy for QE events may be seen in Figs. 8-11 for large kinetic energies. It is interesting to note that for the two isotopes with a mass close to the mass of the projectile, ^{12}B and ^{13}C (Figs. 10 and 11), the ratio decreases as the fragment kinetic energy increases, and it appears that the ratio goes to zero as the fragment velocity approaches the beam velocity. However, for the two isotopes with about half the mass of the projectile, ^{7}Li and ^{8}Li (Figs. 8 and 9), the ratio appears to

be constant, or decreasing slightly, with the ratio still above zero for fragment velocities near the beam velocity. In terms of a nucleon-exchange model, the difference in R versus kinetic energy between IMFs with half-beam mass and near-beam mass is consistent with the picture of collisions with smaller impact parameter (hence more mixing between target and projectile nucleons) for the lower-mass IMFs. Even for IMF velocities near the velocity of the beam, one might expect that the lower-mass IMFs to be in a higher state of excitation than the higher-mass IMFs since a projectile which has lost half of its nucleons is much more deformed than a projectile that has lost only one or two nucleons.

The dependence of R versus kinetic energy was measured for the 6.8-MeV state in ^{11}B and the 4.4-MeV state in ^{12}C for projectilelike fragments created in the E/A = 20 MeV, ^{14}N + ^{164}Dy reaction, and it was found that the ratio was essentially constant with kinetic energy and above zero near the velocity of the beam.[13] Note that these results are quite different from our results for IMFs with similar mass, namely ^{12}B and ^{13}C. In fact, their results more closely resemble our results for ^{7}Li and ^{8}Li. It is not known if the discrepancy between our results and those of Ref. 13 is due to the different beam energy and target or due to the fact that one set of ratios is for unbound states, and the other is for bound states. Regardless, measurements such as these give an indication of the amount of excitation energy deposited in the QE fragment, and the dependence of the ratio on kinetic energy may bear important information on the details of models used to predict the production of QE IMFs, such as the nucleon-exchange model[59] or the participant-spectator model.[12]

B. DI IMFs

The kinetic energy dependence of the ratio of an unbound-state population to a bound-state population for DI IMFs may be seen in Figs. 8 and 9 at 31° and in Fig. 10 for low energies at 15° and 31°. The dependence of the ratio of the 2.255-MeV state population in ^{8}Li (Fig. 9) to the bound-state population on kinetic energy indicates a slightly decreasing or constant ratio with increasing kinetic energy. A constant ratio would be consistent with emission from a thermal source, assuming that effects due to evaporative cooling can be neglected. The data for the 7.46-MeV state in ^{7}Li (Fig. 8) and the 3.388-MeV state in ^{12}B (Fig. 10) are consistent with the dependence of the

ratio on kinetic energy observed for the 2.255-MeV state in ^{8}Li, although there is clearly a need for data at lower fragment kinetic energies to firmly establish this dependence for DI IMFs.

VI. Measured Feeding into Bound States

Although the effects of sequential feeding will alter the measured populations from their initial distributions, very little data exists that measures the magnitude of the feeding into the bound states. Because of this, most analyses have relied on model calculations to correct their data for feeding, just as we have. We have measured the amount of feeding through several neutron-unbound channels into bound states, and we can use this data as a check on the accuracy of feeding calculations we used.

Table II shows the percentage of a bound-state population that came from the decay of a neutron-unbound state. For example, 1.5 % of the ^{11}B bound-state yield at 15° was ^{11}B that came from the decay of the 3.388-MeV state in ^{12}B. The last six columns show the predictions for the amount of feeding according the sequential feeding model calculations, using initial temperatures of 2 MeV, 2.5 MeV, 3 MeV, 3.5 MeV, 4 MeV, and 5 MeV. Most of the data matches the model calculations for an initial temperature between 2.5 and 4 MeV, which is in agreement with the temperatures fitted with the DI population data. The model calculations could not match the data within uncertainties for one case, that being the feeding at 15° from the group of three levels around 7.5 MeV in ^{13}C to the ground state of ^{12}C.

The idea of sequential feeding was first introduced as a possible explanation for the discrepancy between population temperatures and spectral temperatures. It was thought that accounting for the feeding would raise the initial population temperatures enough that they would agree with the spectral temperatures. Although feeding does raise the population temperatures, it is not enough to account for the difference. However, no attempt has been made to see what effect feeding has on the measured spectral temperatures. If the feeding is dependent on the kinetic energy, then correcting the IMF spectra for the feeding will also be energy dependent. This, then, will change the slope of the spectrum, which in turn will have an effect on the deduced spectral temperature.

We were able to measure the dependence of the feeding on kinetic energy in detail for one case, that being the feeding from the 3.388-MeV state in ^{12}B to the ground state of ^{11}B. According to Table II, the best value of the

initial temperature that matches the feeding from both of the detected neutron-unbound states in ^{12}B is ~2.5 MeV. Using that initial temperature, the model predicts that ~33 % of the yield of ^{11}B at 15° and 31° comes from feeding from all of the possible decay channels that end up in a bound state of ^{11}B. The top two plots in Fig. 12 show the fraction of feeding into ^{11}B from the 3.388-MeV state in ^{12}B at 15° and 31° as a function of ^{11}B kinetic energy. The solid lines show a convenient fit to the data. The lower two plots show the measured ^{11}B inclusive spectra at 15° and 31° (open symbols) and the spectra corrected for feeding (solid symbols) using a value of 33 % for total feeding. The dependence of the feeding on kinetic energy for all of the channels was assumed to be the same as the dependence for the one channel which we measured.

The solid lines through the corrected and uncorrected spectra in the lower plots indicate the fits using the sum of two functions. One function was used to fit the DI part of the two spectra at 15° and 31°, and it has the standarad parameterization of a thermal moving source. Equation 3 was used for the other function, which was used to fit the QE part of the data. Only the data at 15° and 31° was used for the fitting. The dotted lines in the lower plots show the contribution from the moving source for the uncorrected data, and the dashed lines show the contribution from the moving source for the corrected data. The value of the temperature of the moving source changed from 11.2 MeV before correcting for feeding to 14.0 MeV after the correction for feeding. The statistical uncertainty of the value of the temperature is less than 5%, in both cases. It appears, then, that correcting for feeding will increase the spectral temperature extracted from ^{11}B singles spectra, just as correcting for feeding will also increase the population temperatures. Based on these results, the effects of sequential feeding cannot account for the discrepancy between population temperatures and spectral temperatures.

VII. SUMMARY

The populations of eleven neutron-unbound states in seven IMFs were measured at 15°, 31°, and 64°, along with the bound-state populations of those seven IMFs. The ratios of unbound-state to bound-state populations for DI IMFs at 15° and 31° were fitted with a statistical sequential decay model using a single initial source temperature between 2.5 and 3.5 MeV. This finding supports the assumption of a statistical, or thermal, origin for DI IMFs. However, at 64°, where all of the IMFs come from DI reactions, fits to

most of the measured population ratios were not possible with the sequential decay model. Although the DI and QE reaction mechanisms are quite different, there was basically no difference between QE and DI two-level population ratios for most IMFs.

It is possible to fit the populations of four groups of states detected in ^{13}C (bound states + 3 groups of unbound states) with a single temperature at 15° and $E_{^{13}C} \leq$ 15 MeV/nucleon. This is additional evidence of a thermal origin of DI IMFs. Also, above 15 MeV/nucleon, where QE reactions dominate, the four groups of populations in ^{13}C cannot be fitted. However, we could not fit the populations of three groups of states in ^{12}B (bound states + 2 unbound states) with a single temperature for either DI or QE reactions.

The functional dependence of the ratio of a neutron-unbound state population to a bound-state population on IMF kinetic energy was investigated for several QE and DI IMFs. For QE IMFs close to the projectile mass, the ratio decreased with increasing kinetic energy, going to zero as the fragment velocity approached the beam velocity. However, for QE IMFs with about half the mass of the projectile, the ratio only slightly decreased with increasing velocity, and stayed above zero at velocities near the beam velocity. For DI IMFs, the measured ratios can be approximated with a constant functional dependence, but there is a need for data below our threshold (6 MeV/nucleon) in order to draw any firm conclusions about the dependence. A constant functional dependence is consistent with emission from a thermal source.

The amount of feeding into bound states was measured for several neutron decay channels. The data is consistent with predictions of the feeding from a sequential decay model. Comparisons of the measured feeding and the predicted feeding from a sequential decay model indicate a source temperature between 2.5 and 4.0 MeV, which is consistent with the temperatures deduced from the analysis of two-level population ratios. The functional dependence of the amount of feeding on IMF kinetic energy was also investigated, and this dependence was used to estimate the correction to the ^{11}B inclusive spectra at 15° and 31°. Correcting for feeding raised the spectral temperature extracted from a moving-source analysis of the ^{11}B spectra from 11.2 MeV to 14.0 MeV

VIII. CONCLUSIONS

The ratios of neutron-unbound state populations to bound-state populations in DI IMFs are in general agreement with model calculations that assume a thermal mechanism for their production. Some of the DI population

ratios are not fitted with the model calculations, however, which may suggest that other effects are present in the DI reaction mechanism that are not accounted for in the thermal, sequential decay model. The dependence of the ratio of an unbound-state population to its bound-state population on kinetic energy is consistent with emission from a thermal source, but additional data is needed to come to a definite conclusion. Correcting both the unbound-state populations and inclusive spectra for feeding does not resolve the discrepancy between population temperatures derived from state populations and spectral temperatures derived from moving source analyses of singles spectra.

No clear difference can be seen between the two-level population ratios of DI and QE IMFs, where the data was sorted into relatively broad cuts on IMF kinetic energy. However, a difference between QE and DI IMFs can be seen in the dependence of the population ratios on narrower cuts on IMF kinetic energy. In addition, a difference in the dependence of the population ratio on kinetic energy is observed between half-beam mass and near-beam mass IMFs.

Table I - Percentage of QE fragments as determined by fits to inclusive IMF spectra using Eqs. 2 and 3 of the text for various cuts on IMF kinetic energy (in MeV) at 15° and 31°. Typical uncertainties of the fits are from ± 1% to ± 3%.

isotope	15° $E/A \geq 15$	15° $6 \leq E/A \leq 15$	15° $6 \leq E/A \leq 10$	31° $E/A \geq 6$	31° $6 \leq E/A \leq 15$
^{7}Li	87 %	37 %	26 %	7 %	2 %
^{8}Li	94 %	55 %	43 %	5 %	2 %
^{10}Be	92 %	22 %	11 %	24 %	11 %
^{12}B	90 %	14 %	6 %	19 %	8 %
^{12}C	97 %	31 %	16 %	15 %	6 %
^{13}C	96 %	25 %	12 %	10 %	5 %
^{14}C	94 %	18 %	9 %	7 %	6 %

Table II- Percent feeding from neutron-unbound states into their corresponding daughter-fragment inclusive yields at various angles. The uncertainty in the last significant digit(s) is enclosed in the parenthesis following the value of the feeding. The last 6 columns show predictions for the percent feeding from a sequential feeding calculation described in the text. The initial temperature used in the calculation is indicated in the column heading.

parent state	θ	exp % feeding	model 2 MeV	model 2.5 MeV	model 3 MeV	model 3.5 MeV	model 4 Mev	model 5 MeV
^{7}Li(7.46)	15°	5.0(3)	2.1	5.1	8.7	12.3	15.4	20.5
^{7}Li(7.46)	31°	5.0(3)	2.2	5.1	8.7	12.3	16.0	21.6
^{7}Li(7.46)	64°	8.7(7)	2.2	5.3	9.0	13.2	16.5	21.6
^{8}Li(2.255)	15°	6.6(3)	1.2	2.8	4.7	6.8	8.6	11.7
^{8}Li(2.255)	31°	9.3(5)	1.2	2.8	4.8	6.8	9.0	12.3
^{8}Li(2.255)	64°	7.6(5)	1.2	2.9	5.0	7.4	9.3	12.3
^{9}Li(4.296)	15°	4.3(10)	0.5	1.2	2.1	3.1	4.1	5.8
^{9}Li(4.296)	31°	3.8(10)	0.5	1.2	2.1	3.1	4.1	5.8
^{8}Be(19.23)	15°	4.0(2)	1.5	3.6	6.1	9.0	11.9	17.3
^{8}Be(19.23)	31°	3.1(3)	1.5	3.6	6.2	9.0	11.9	17.1
^{10}Be(7.5)	15°	6.6(6)	2.3	5.7	9.5	13.1	15.7	18.7
^{10}Be(7.5)	31°	6.5(6)	2.4	5.7	9.7	13.1	16.3	20.0
^{10}Be(7.5)	64°	4.9(6)	2.4	5.8	9.9	14.0	16.8	20.0
^{10}Be(9.5)	15°	6.(2)	1.	3.	6.	9.	11.	14.
^{10}Be(9.5)	31°	4.2(12)	1.1	3.1	6.0	8.8	11.6	15.1
Σ^{10}Be	15°	12.(2)	3.	9.	15.	22.	27.	33.
Σ^{10}Be	31°	10.7(13)	3.4	8.8	15.6	22.0	27.9	35.1
^{11}Be(3.89)	15°	1.20(4)	0.13	0.34	0.61	0.91	1.21	1.75
^{11}Be(3.89)	31°	0.80(4)	0.13	0.34	0.62	0.91	1.23	1.82
^{11}Be(3.89)	64°	1.3(3)	0.1	0.4	0.6	0.9	1.3	1.8
^{11}Be(3.96)	15°	1.10(14)	0.25	0.66	1.19	1.78	2.35	3.38
^{11}Be(3.96)	31°	0.60(11)	0.26	0.66	1.20	1.78	2.41	3.52
Σ^{11}Be	15°	2.69(14)	0.38	1.00	1.80	2.69	3.56	5.13

Table II- continued

parent state	θ	exp % feeding	model 2 MeV	model 2.5 MeV	model 3 MeV	model 3.5 MeV	model 4 Mev	model 5 MeV
Σ^{11}Be	31°	1.30(12)	0.39	1.00	1.82	2.69	3.64	5.34
^{12}B(3.388)	15°	1.50(3)	1.15	2.03	2.55	2.82	2.80	2.56
^{12}B(3.388)	31°	1.60(4)	1.17	2.03	2.61	2.82	2.92	2.76
^{12}B(3.388)	64°	2.7(3)	1.2	2.1	2.7	3.1	3.0	2.8
^{12}B(3.76)	15°	1.70(18)	0.68	1.27	1.67	1.94	2.04	2.12
^{12}B(3.76)	31°	1.3(2)	0.7	1.3	1.7	1.9	2.1	2.3
Σ^{12}B	15°	3.20(18)	1.83	3.30	4.22	4.76	4.84	4.68
Σ^{12}B	31°	2.9(2)	1.9	3.3	4.3	4.8	5.0	5.0
^{13}C(6.86)	15°	2.7(8)	1.9	3.7	4.8	5.3	5.1	4.6
^{13}C(6.86)	31°	1.4(13)	1.9	3.7	5.0	5.3	5.5	5.4
^{13}C(7.5)	15°	16.(2)	4.	8.	11.	13.	12.	11.
^{13}C(7.5)	31°	12.(3)	4.	8.	12.	13.	13.	13.
^{13}C(9.5)	15°	1.50(8)	0.81	1.95	2.64	2.78	2.41	1.78
^{13}C(9.5)	31°	1.9(2)	0.8	2.0	2.7	2.8	2.7	2.2
^{13}C(9.5)	64°	3.5(12)	0.8	2.1	2.9	3.3	2.9	2.2
Σ^{13}C	15°	21.(2)	7.	14.	19.	21.	20.	18.
Σ^{13}C	31°	16.(3)	7.	14.	20.	21.	22.	20.
^{14}C(8.32)	15°	1.10(12)	1.25	2.10	2.51	2.72	2.68	2.56
^{14}C(8.32)	31°	1.6(2)	1.3	2.1	2.6	2.7	2.9	2.9

References

* - Permanent Address: Physics Department, Kyoto University, Kyoto 606, Japan

† - While on leave from Centro Tecnico Aeroespacial and State of São Paulo Foundation for Support of Research (FAPESP), Brazil

1 - J. Mougey, R. Ost, M. Buenerd, A. J. Cole, C. Guet, D. Lebrun, J. M. Loiseaux, P. Martin, M. Maurel, E. Monnand, H. Nifenecker, P. Perrin, J. Pinston, C. Ristori, P. de Saintignon, F. Schussler, L. Carlen, B. Jakobsson, A. Oskarsson, I. Otterlund, B. Schroder, H. A. Gustafsson, T. Johansson, H. Ryde, J. P. Bondorf, O. B. Nielsen, and G. Tibell, Phys. Lett. **105B**, 25 (1981).

2 - A. Menchaca-Rocha, M. E. Brandan, M. Buenerd, J. Chauvin, D. Lebrun, P. Martin, P. de Santignon, J. C. Gondrand, I. Dorion, and A. Lounis, Phys. Lett. **131B**, 31 (1983).

3 - D. Guerreau, V. Borrel, D. Jacquet, J. Galin, B. Gatty, and X. Tarrago, Phys. Lett. **131B**, 293 (1983).

4 - M. N. Namboodiri, R. K. Choudhury, J. B. Natowitz, K. Hagel, L. Adler, P. L. Gonthier, H. Simon, S. Kniffen, R. Patton, E. Tomasi, C. Ngo, C. Mazur, and M. Ribrag, Phys. Rev. C **28**, 460 (1983).

5 - M. J. Murphy and R. G. Stokstad, Phys. Rev. C **28**, 428 (1983).

6 - Y. Blumenfeld, Ph. Chomaz, N. Frascaria, J. P. Garron, J. C. Jacmart, J. C. Roynette, D. Ardouin, and W. Mittig, Nucl. Phys. **A455**, 357 (1986).

7 - G. Caskey, L. Heilbronn, B. Remington, A. Galonsky, F. Deák, A. Kiss, and Z. Seres, Phys. Rev. C **37**, 969 (1988).

8 - A. Kiss, F. Deák, Z. Seres, G. Caskey, A. Galonsky, B. Remington, and L. Heilbronn, Nucl. Phys. **A499**, 131 (1989).

9 - F. Deák, A. Kiss, Z. Seres, A. Galonsky, L. Heilbronn, and H. R. Schelin, Phys. Rev. C **42**, 1029 (1990).

10 - A. S. Goldhaber, Phys. Lett. **53b**, 306 (1974).

11 - W. A. Friedman, Phys. Rev. C **27**, 569 (1983).

12 - F. Deák, A. Kiss, Z. Seres, A. Galonsky, C. K. Gelbke, L. Heilbronn, W. Lynch, T. Murakami, H. Schelin, M. B. Tsang, B. A. Remington, and J. Kasagi, Phys. Rev. C **39**, 733 (1989).

13 - K. Siwek-Wilczynska, R. A. Blue, L. H. Harwood, R. M. Ronningen, H. Utsunomiya, J. Wilczynski, and D. J. Morrissey, Phys. Rev. C **32**, 1450 (1985).

14 - P. J. Siemens, J. P. Bondorf, D. H. E. Gross, and F. Dickman, Phys. Lett. **36B**, 24 (1971).

15 - J. Wilczynski and K. Siwek-Wilczynska, Phys. Rev. C **41**, R1917 (1990).

16 - Z. Chen, C. K. Gelbke, W. G. Gong, Y. D. Kim, W. G. Lynch, M. R. Maier, J. Pochodzalla, M. B. Tsang, F. Saint-Laurent, D. Ardouin, H. Delagrange, H. Doubre, J. Kasagi, A. Kyanowski, A. Peghaire, J. Peter, E. Rosato, G. Bizard, F. Lefebvres, B. Tamain, J. Quebert, and Y. P. Viyogi, Phys. Rev. C. **36**, 2297 (1987).

17 - Z. Chen, C. K. Gelbke, J. Pochodzalla, C. B. Chitwood, D. J. Fields, W. G. Gong, W. G. Lynch, and M. B. Tsang, Nucl. Phys. **A473** 564 (1987).

18 - Z. Chen, Ph.D. Thesis, Michigan State University.

19 - C. Bloch, W. Benenson, A. I. Galonsky, E. Kashy, J. Heltsley, L. Heilbronn, M. Lowe, R. J. Radtke, B. Remington, J. Kasagi, and D. J. Morrissey, Phys. Rev. C **37**, 2469 (1988).

20 - D. Fox, D. A. Cebra, J. Karn, C. Parks, A. Pradhan, A. Vander Molen, J. van der Plicht, G. D. Westfall, W. K. Wilson, and R. S. Tickle, Phys. Rev. C **38**, 146 (1988).

21 - J. Pochodzalla, C. K. Gelbke, W. G. Lynch, M. Maier, D. Ardouin, H. Delagrange, H. Doubre, C. Gregoire, A. Kyanowski, W. Mittig, A. Péghaire, J. Péter, F. Saint-Laurent, B. Zwieglinski, G. Bizard, F. Lefèbvres, B. Tamain, J. Quèbert, Y. P. Viyogi, W. A. Friedman, and D. H. Boal, Phys. Rev. C **35**, 1695 (1987).

22 - G. D. Westfall, J. Gosset, P. J. Johansen, A. M. Poskanzer, and W. G. Meyer, Phys. Rev. Lett **37**, 1202 (1976).

23 - D. J. Morrissey, W. Benenson, E. Kashy, B. Sherrill, A. D. Panagiotou, R. A. Blue, R. M. Ronningen, J. van der Plicht, and H. Utsunomiya, Phys. Lett. **148B**, 423 (1984).

24 - D. J. Morrissey, W. Benenson, E. Kashy, C. Bloch, M. Lowe, R. A. Blue, R. M. Ronningen, B. Sherrill, H. Utsunomiya, and I. Kelson, Phys. Rev. C **32**, 877 (1985).

25 - C. Bloch, W. Benenson, A. I. Galonsky, E. Kashy, J. Heltsley, L. Heilbronn, M. Lowe, B. Remington, D. J. Morrissey, and J. Kasgi, Phys. Rev. C **36**, 203 (1987).

26 - J. Gomez del Campo, J. L. Charvet, A. D'Onofrio, R. L. Auble, J. R. Beene, M. L. Halbert, and H. J. Kim, Phys. Rev. Lett. **61**, 290 (1988).

27 - H. M. Xu, W. G. Lynch, C. K. Gelbke, M. B. Tsang, D. J. Fields, M. R. Maier, D. J. Morrissey, T. K. Nayak, J. Pochadzalla, D. G. Sarantites, L. G. Sobotka, M. L. Halbert, and D. C. Hensley, Phys. Rev. C **40**, 186 (1989).

28 - J. Pochodzalla, W. A. Friedman, C. K. Gelbke, W. G. Lynch, M. Maier, D. Ardouin, H. Delagrange, H. Doubre, C. Gregoire, A. Kyanowski, W. Mittig, A. Péghaire, J. Péter, F. Saint-Laurent, Y. P. Viyogi, B. Zwieglinski, G. Bizard, F. Lefèbvres, B. Tamain, and J. Quèbert, Phys. Rev. Lett. **55**, 177 (1985).

29 - J. Pochodzalla, W. A. Friedman, C. K. Gelbke, W. G. Lynch, M. Maier, D. Ardouin, H. Delagrange, H. Doubre, C. Gregoire, A. Kyanowski, W. Mittig, A. Péghaire, J. Péter, F. Saint-Laurent, Y. P. Viyogi, B. Zwieglinski, G. Bizard, F. Lefèbvres, B. Tamain, and J. Quebért, Phys. Lett. **161B**, 275 (1985).

30 - C. B. Chitwood, C. K. Gelbke, J. Pochodzalla, Z. Chen, D. J. Fields, W. G. Lynch, R. Morse, M. B. Tsang, D. H. Boal, and J. C. Shillcock, Phys. Lett. **172B**, 27 (1986).

31 - H. M. Xu, D. J. Fields, W. G. Lynch, M. B. Tsang, C. K. Gelbke, M. R. Maier, D. J. Morrissey, J. Pochodzalla, D. G. Sarantites, L. G. Sobotka, M. L. Halbert, D. C. Hensley, D. Hahn, and H. Stöcker, Phys. Lett. **182B**, 155 (1986).

32 - A. Kiss, F. Deák, Z. Seres, G. Caskey, A. Galonsky, L. Heilbronn, B. A. Remington, and J. Kasagi, Phys. Lett. **184B**, 149 (1987).

33 - A. Galonsky, G. Caskey, L. Heilbronn, B. Remington, H. Schelin, F. Deák, A. Kiss, Z. Seres, and J. Kasagi, Phys. Lett. **197B**, 511 (1987).

34 - Z. Chen, C. K. Gelbke, W. G. Gong, Y. D. Kim, W. G. Lynch, M. R. Maier, J. Pochodzalla, M. B. Tsang, F. Saint-Laurent, D. Ardouin, H. Delagrange, H. Doubre, J. Kasagi, A. Kyanowski, A. Péghaire, J. Péter, E. Rosato, G. Bizard, F. Lefèbvres, B. Tamain, J. Quèbert, and Y. P. Viyogi, Phys. Lett. B **199** 171 (1987).

35 - F. Saint-Laurent, A. Kyanowski, D. Ardouin, H. Delagrange, H. Doubre, C. Gregoire, W. Mittig, A. Péghaire, J. Péter, G. Bizard, F. Lefèbvres, B. Tamain, J. Quèbert, Y. P. Viyogi, J. Pochodzalla, C. K. Gelbke, W. Lynch, and M. Maier, Phys. Lett. **202B**, 190 (1988).

36 - T. K. Nayak, T. Murakami, W. G. Lynch, K. Swartz, D. J. Fields, C. K. Gelbke, Y. D. Kim, J. Pochodzalla, M. B. Tsang, H. M. Xu, F. Zhu, and K. Kwiatkowski, Phys. Rev. Lett. **62**, 1021 (1989).

37 - D. A. Cebra, W. Benenson, Y. Chen, E. Kashy, A. Pradhan, A. Vander Molen, G. D. Westfall, W. K. Wilson, D. J. Morrissey, R. S. Tickle, R. Korteling, and R. L. Helmer, Phys. Lett. **227B**, 336 (1989).

38 - D. Hahn and H. Stöcker, Phys. Rev. C **35**, 1311 (1987).

39 - Jeong Ho Lee, W. Benenson, and D. J. Morrissey, Phys. Rev. C **41**, 1562 (1990).

40 - J. H. Lee, W. Benenson, C. Bloch, Y. Chen, R. J. Radtke, E. Kashy, M. F. Mohar, D. J. Morrissey, R. Blue, and R. M. Ronningen, Phys. Rev. C **41**, 2406 (1990).

41 - F. Deák, A. Kiss, Z. Seres, G. Caskey, A. Galonsky, and B. Remington, Nucl. Instrum. Methods **A258**, 67 (1987).

42 - J. Heltsley, L. Brandon, A. Galonsky, L. Heilbronn, B. A. Remington, S. Langer, A. Vander Molen, J. Yurkon, and J. Kasagi, Nucl. Instrum. and Methods **A263**, 441 (1988).

43 - R. J. Kurz, University of California Radiation Lab Internal Report URCL-11339 (1964).

44 - R. A. Cecil, B. D. Anderson, and R. Madey, Nucl. Instrum. and Methods **161**, 439 (1979).

45 - B. A. Remington, Ph.D. Thesis, Michigan State University (1986).

46 - T. Nayak, Ph.D. thesis, Mich. State Univ. (1990).

47 - F. Ajzenberg-Selove, Nucl. Phys. **A413**, 1 (1984).

48 - J. E. Monahan, L. C. Biedenharn, and J. P. Schiffer, Argonne National Laboratory, ANL-5846 (1958).

49 - G. J. Wozniak, H. L. Harney, K. H. Wilcox, and J. Cerny, Phys. Rev. Lett. **28**, 1278 (1972).

50 - C. Bloch, W. Benenson, E. Kashy, D. J. Morrissey, R. A. Blue, R. M. Ronningen, and H. Utsunomiya, Phys. Rev. C **34**, 850 (1986).

51 - F. Ajzenberg-Selove, Nucl. Phys. **A449**, 1 (1986).

52 - F. Ajzenberg-Selove, Nucl. Phys. **A506**, 1 (1990).

53 - L. Heilbronn, A. Galonsky, X. Yang, F. Deák, A. Kiss, and Z. Seres, Phys. Rev. C **40**, 2576 (1989).

54 - P. G. Young and R. H. Stokes, Phys. Rev. C **4**, 1597 (1971).

55 - V. McLane, C. L. Dunford, and P. F. Rose, Neutron Cross Sections, (Academic Press, San Diego, 1988), Vol. 2.

56 - H. Ohnuma, N. Hoshino, O. Mikoshiba, K. Raywood, A. Sakaguchi, G. G. Shute, B. M. Spicer, M. H. Tanaka, M. Tanifuji, T. Terasawa, and M. Yasue, Nucl. Phys. **A448**, 205 (1986).

57 - W. Hauser and H. Feshbach, Phys. Rev. **87**, 366 (1952).

58 - D. Boal, Phys. Rev. C **30**, 749 (1980).

59 - J. Wilczynski and H. W. Wilschut, Phys. Rev. C **39**, 2475 (1989).

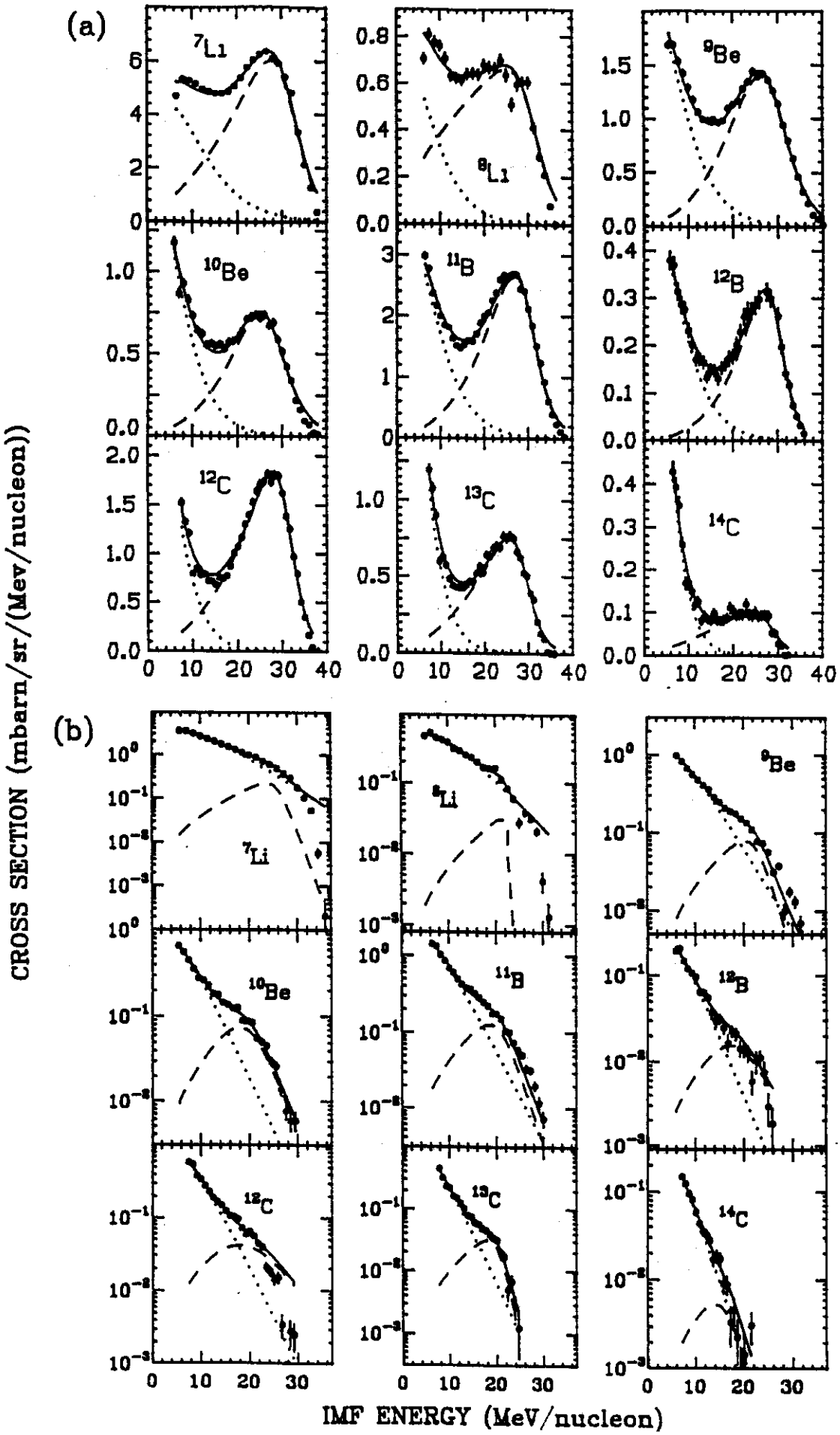

Fig. 1 - Fragment singles spectra for 15° (a) and 31° (b). The solid, dotted and dashed lines are from a fit explained in the text.

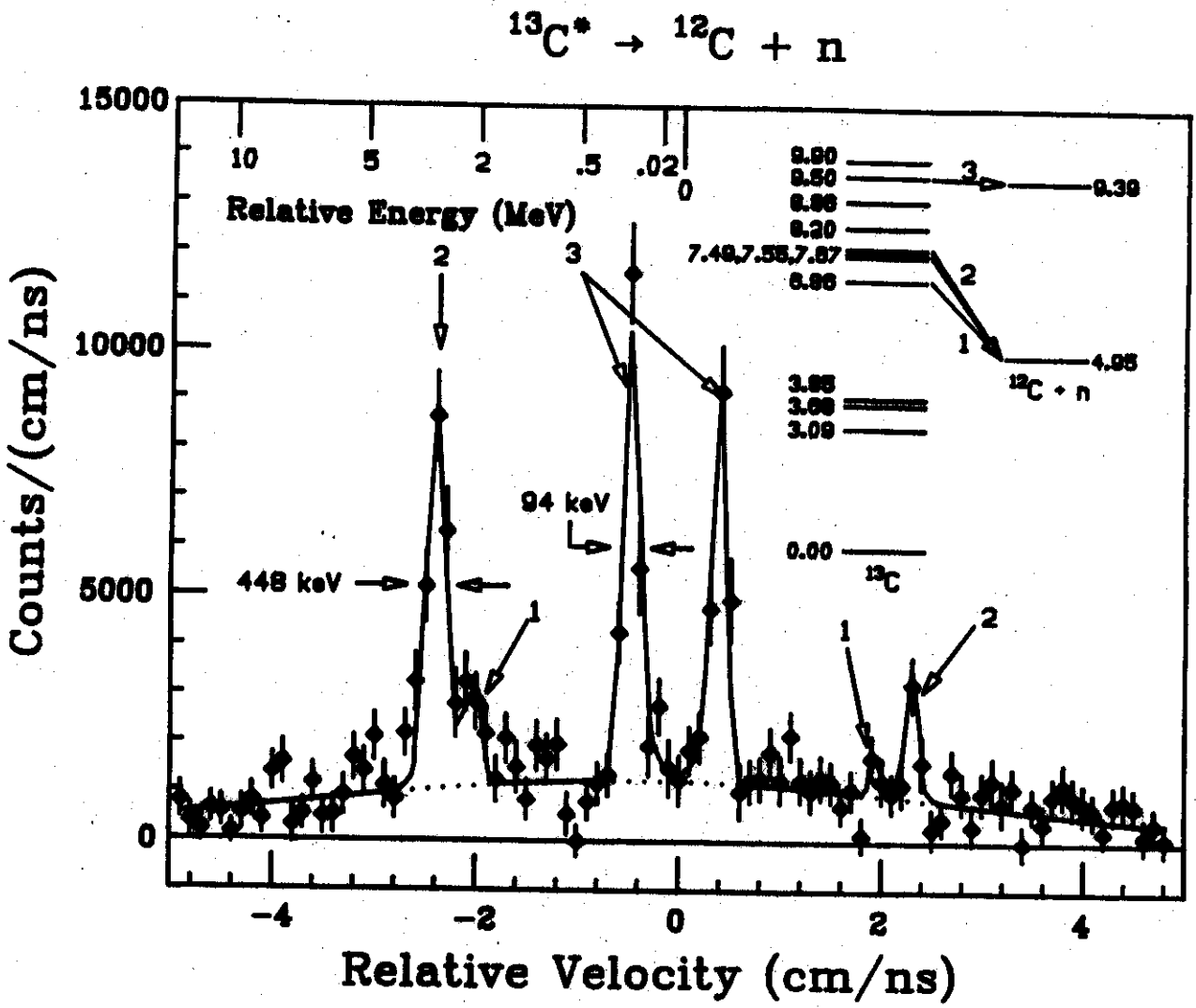

Fig. 2 - Relative velocity spectrum for $^{12}C + n$ at 15° and for $E_{^{12}C} \geq 15$ MeV/nucleon. The numbered resonances come from the decays indicated in the level diagram. A relative energy scale is included for reference. The FWHM of peaks 2 and 3 are given. Each width corresponds to relative velocity resolution of 2 cm/ns. The solid line is from a fit described in the text, and the dotted line shows the background used in the fit (a Gaussian).

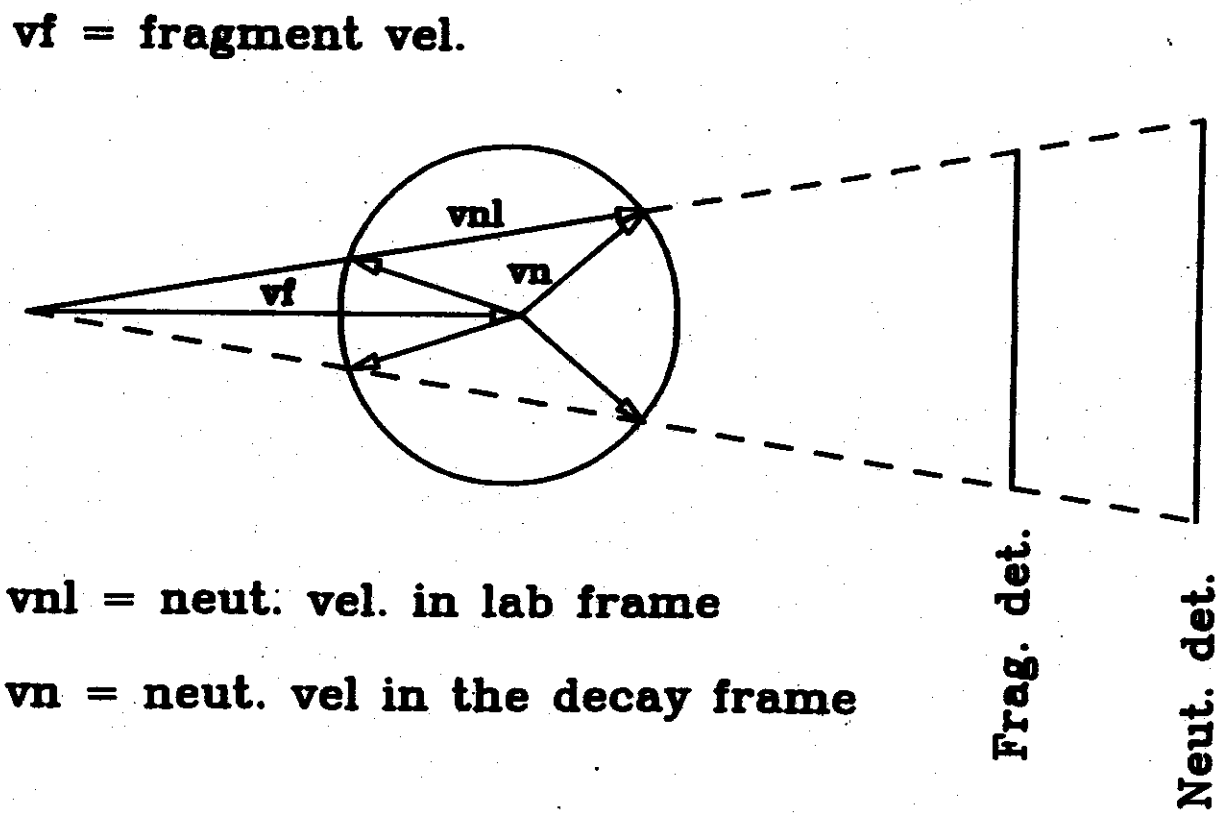

Fig. 3 - A velocity diagram showing the neutron decay of an excited fragment heading towards a colinear fragment-neutron detection system. Recoil of the daughter is neglected. The dashed line indicates the cone of acceptance of the detection system, and the circle represents all of the possible directions of decay. Only decays that lie within the cone of acceptance will be detected.

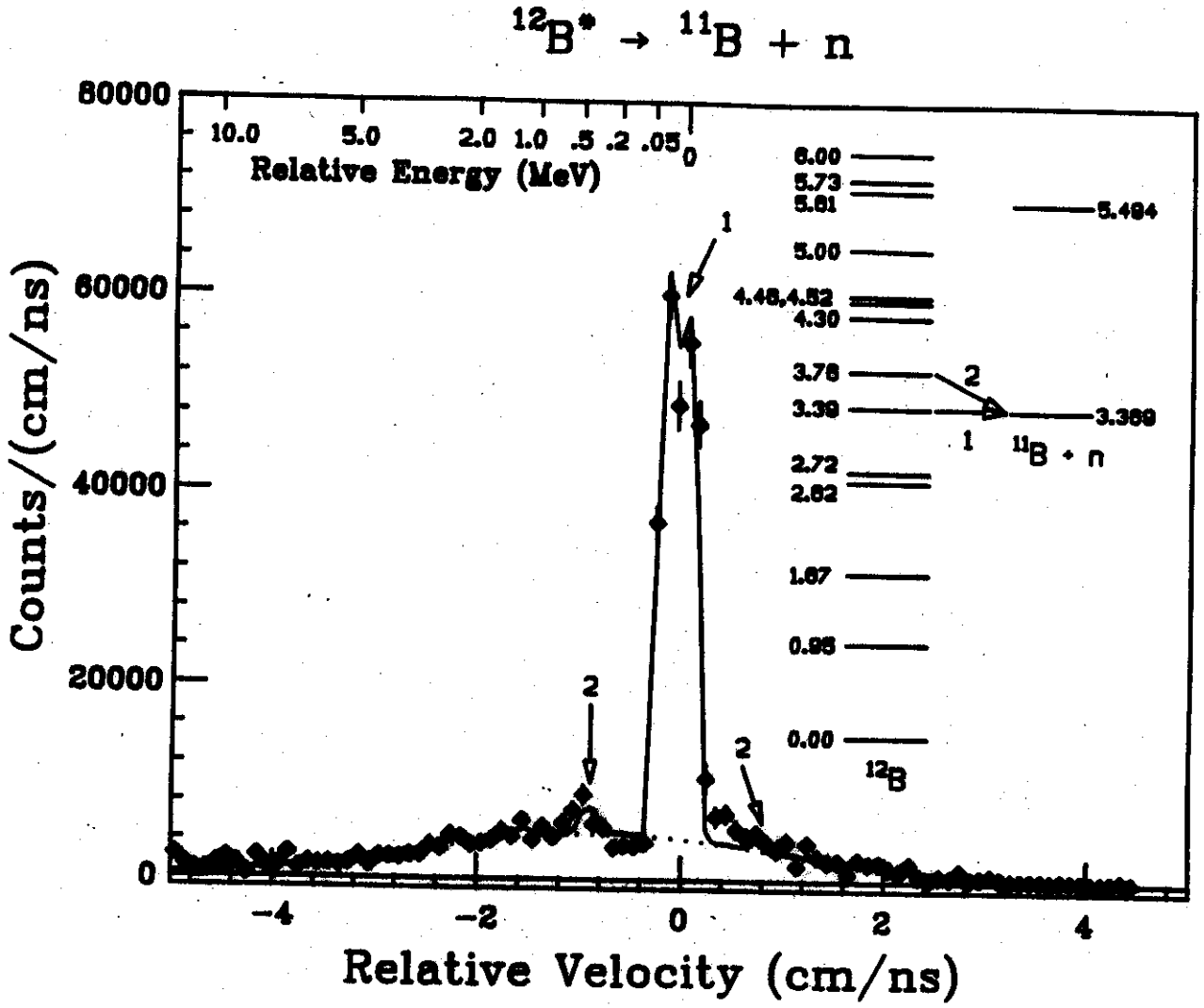

Fig. 4 - Relative velocity spectrum for $^{11}B + n$ at 31° and for $E_{^{11}B} \geq 6$ MeV/nucleon. The numbered locations correspond to relative velocities that come from the decays indicated in the energy level diagram. A relative energy scale is included for reference. The solid line is from a fit described in the text, and the dotted line shows the background used in the fit (a Gaussian).

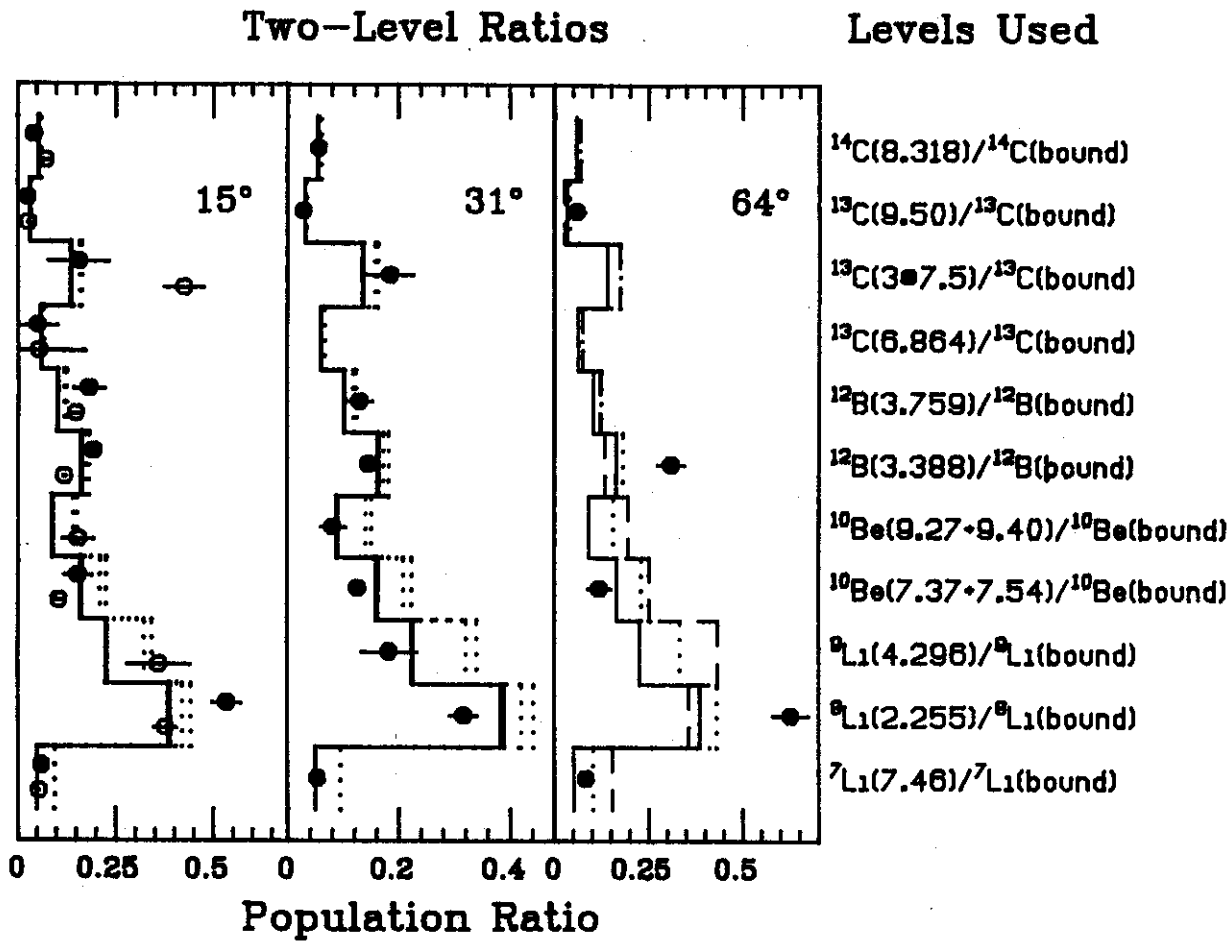

Fig. 5 - The lefthand plot contains the population ratios at 15° with the solid symbols representing the DI data and the open symbols representing the QE data. The middle plot is for DI IMFs at 31°, and the righthand plot is for DI IMFs at 64°. The solid histograms in every plot indicate the ratios calculated from a sequential feeding model for T_{source}= 2.5 MeV, and the dotted histograms indicate the calculated ratios for T_{source}= 3.5 MeV. The dashed line in the righthand plot indicates the ratios predicted by the sequential feeding model for T_{source}= 6.0 MeV. The bound states and unbound states used to calculate the ratios are shown on the righthand side of the figure.

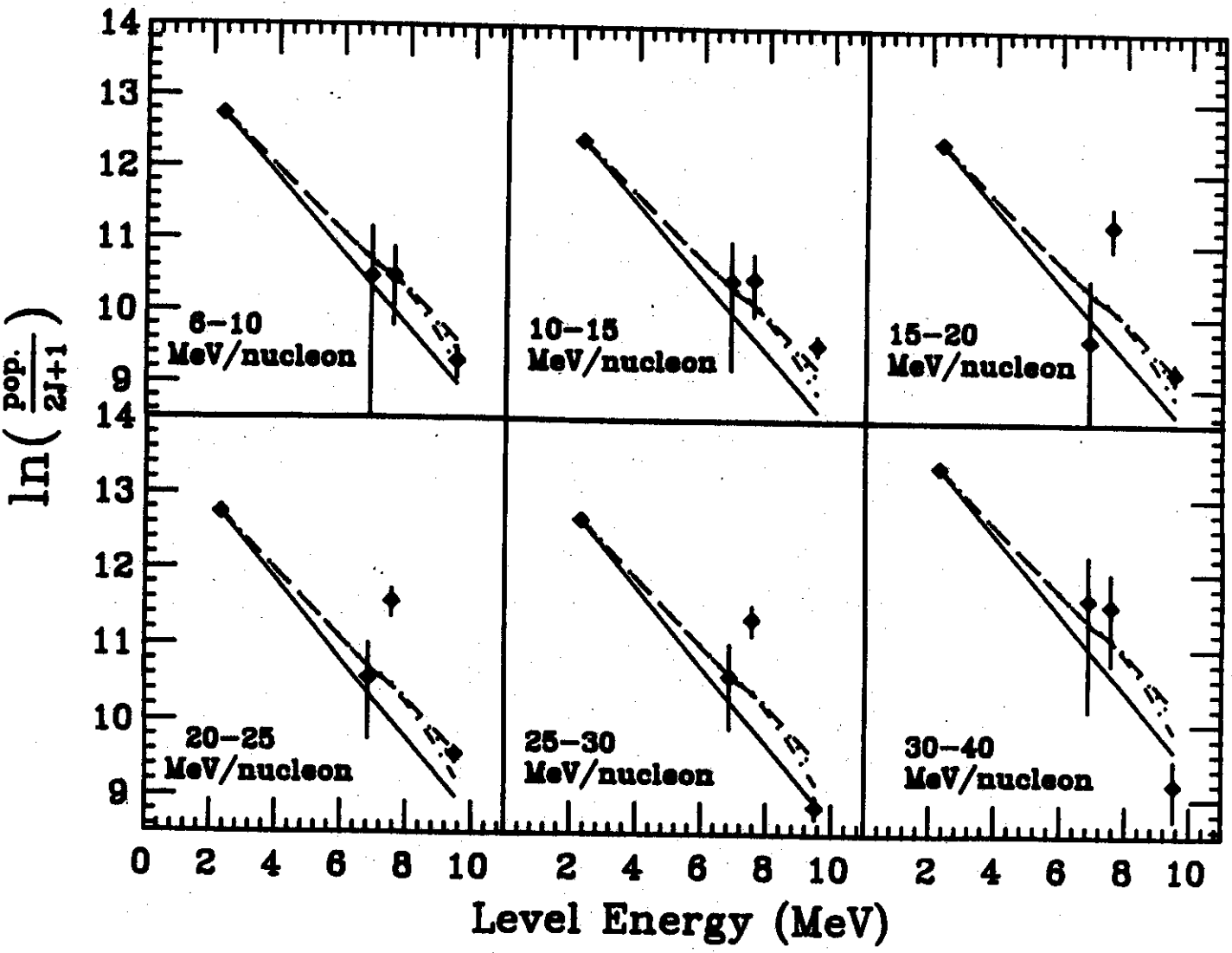

Fig. 6 - Plots of the natural logarithm of the populations of the detected levels in ^{13}C vs. the level energy for various cuts on fragment kinetic energy. The solid, dashed, dotted, and dot-dashed lines in each plot show the predictions from the sequential feeding model for initial source temperatures of 2, 3, 4, and 5 MeV, respectively.

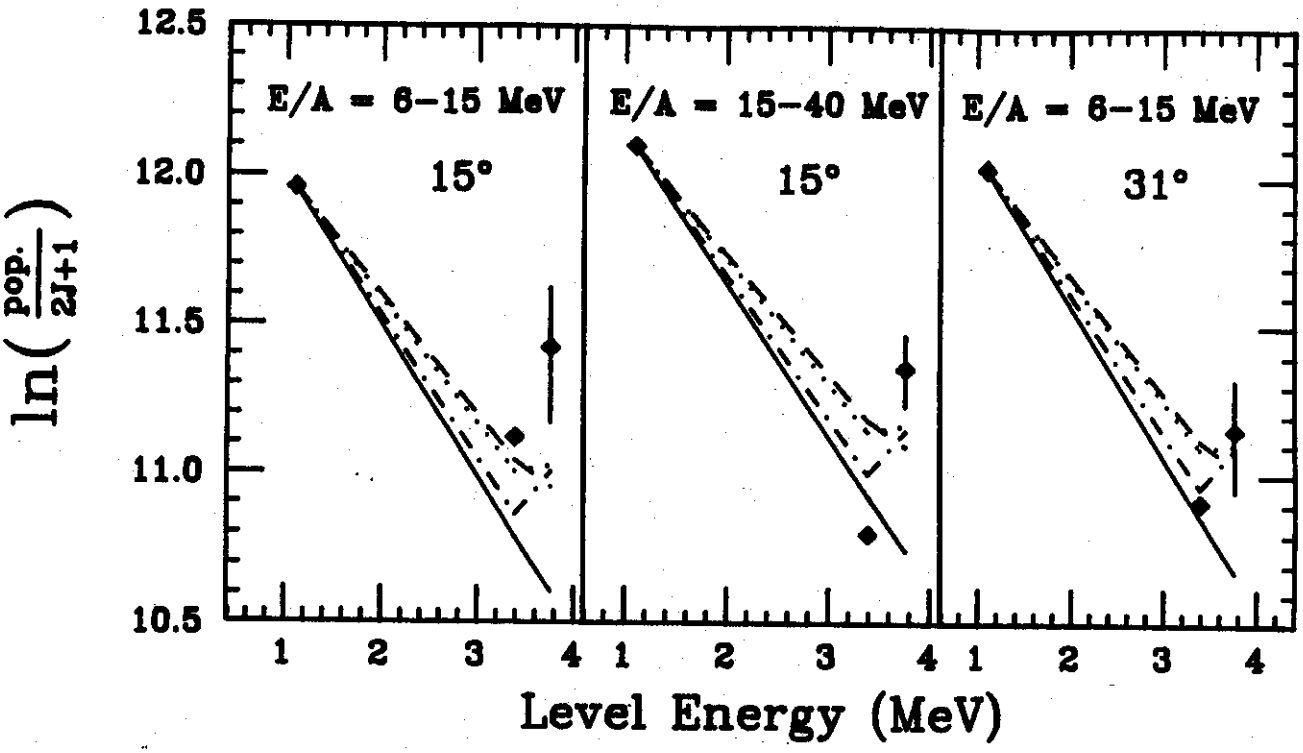

Fig. 7 - Plots of the natural logarithm of the populations of the detected levels in ^{12}B vs. the level energy for various cuts on IMF energy at 15° and 31°. The lines have the same meaning as in Fig. 6.

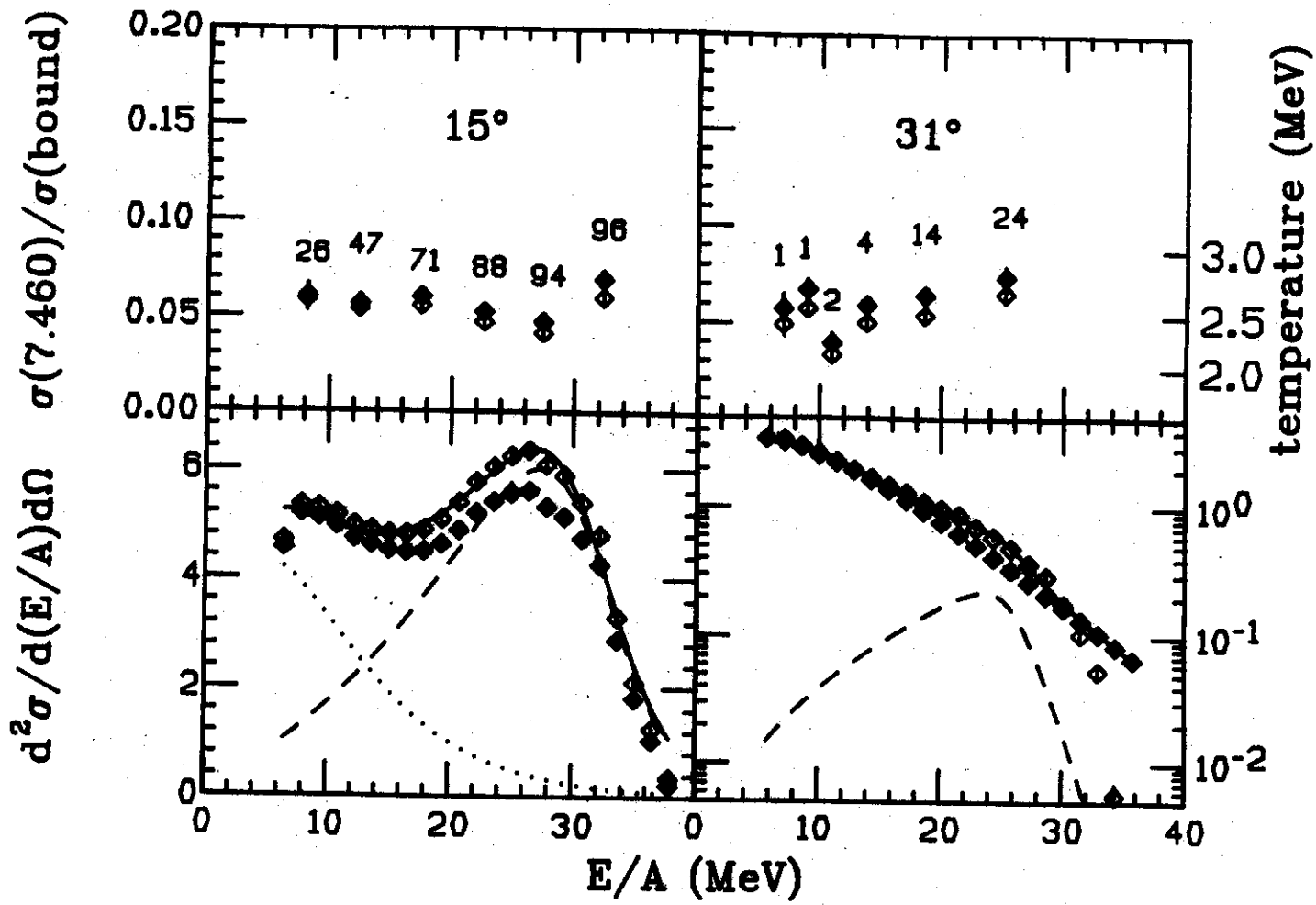

Fig. 8 - The upper plots show the ratio of the population of the neutron-unbound 7.46-MeV state in ^{7}Li to the ^{7}Li bound-state population as a function of fragment kinetic energy at 15° and 31°. Open symbols represent the data before correcting for ^{8}Be contamination, and filled symbols represent the data after the correction. The temperature scale on the right hand side was deduced from Eq. 1. The lower plots show the ^{7}Li singles spectra at 15° and 31°. The open and filled symbols have the same meanings as for the upper plots. The solid, dotted, and dashed lines are from a fit described in the text. The numbers in the upper two plots indicate the percentage of QE ^{7}Li in the bound-state yield for the corresponding energy bin.

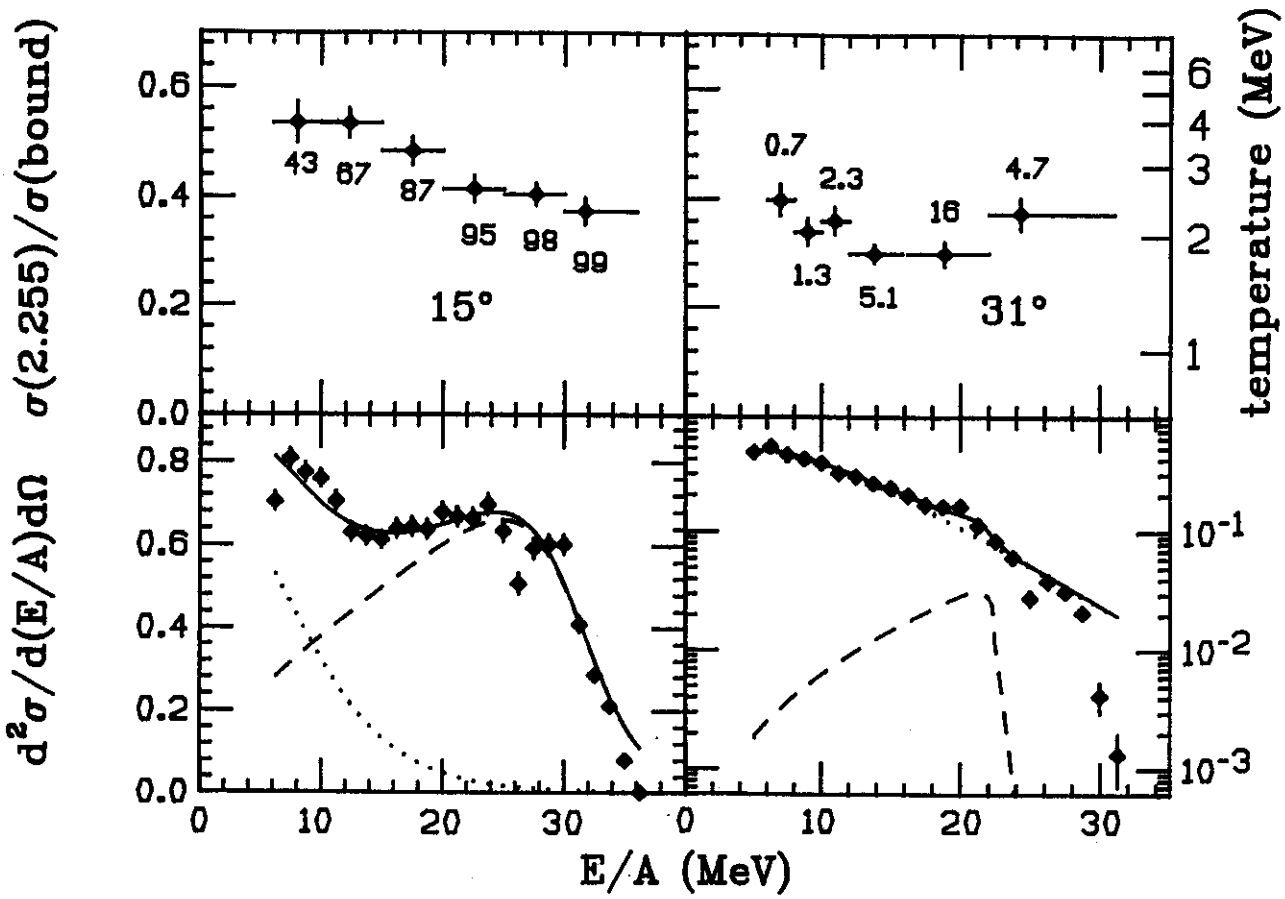

Fig. 9 - The upper plots show the ratio of the population of the neutron-unbound 2.255-MeV state in ^{8}Li to the ^{8}Li bound-state population as a function of fragment kinetic energy at 15° and 31°. The lower plots show ^{8}Li singles spectra at 15° and 31°. The solid, dotted, and dashed lines are from a fit described in the text. The numbers in the upper two plots indicate the percentage of QE ^{8}Li in the bound-state yield for the corresponding energy bin.

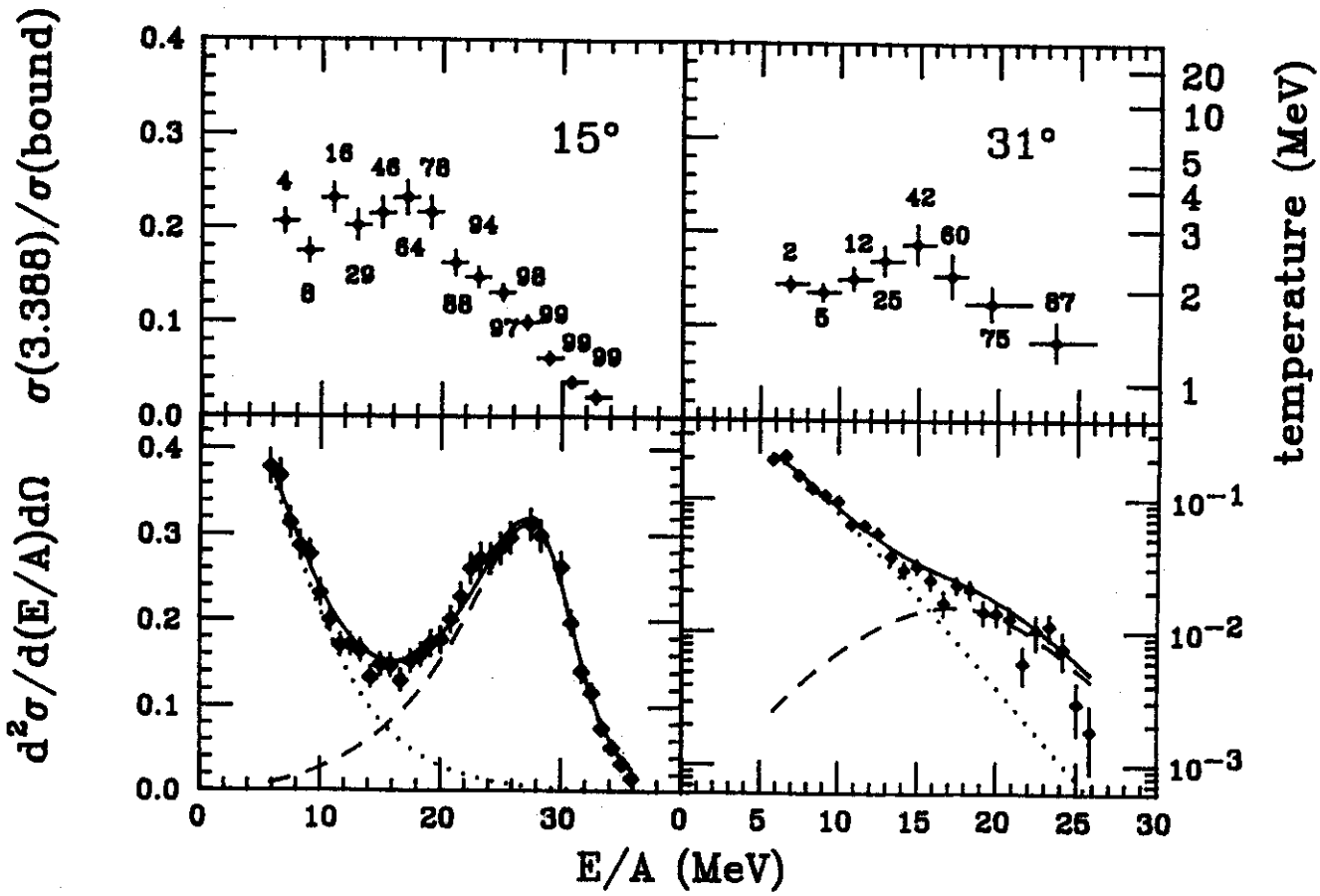

Fig. 10 - The upper plots show the ratio of the population of the neutron-unbound 3.388-MeV state in ^{12}B to the ^{12}B bound-state population as a function of fragment kinetic energy at 15° and 31°. The lower plots show ^{12}B singles spectra at 15° and 31°. The solid, dotted, and dashed lines are from fits described in the text. The numbers in the upper plots indicate the percentage of QE ^{12}B in the bound-state yield for the corresponding energy bin.

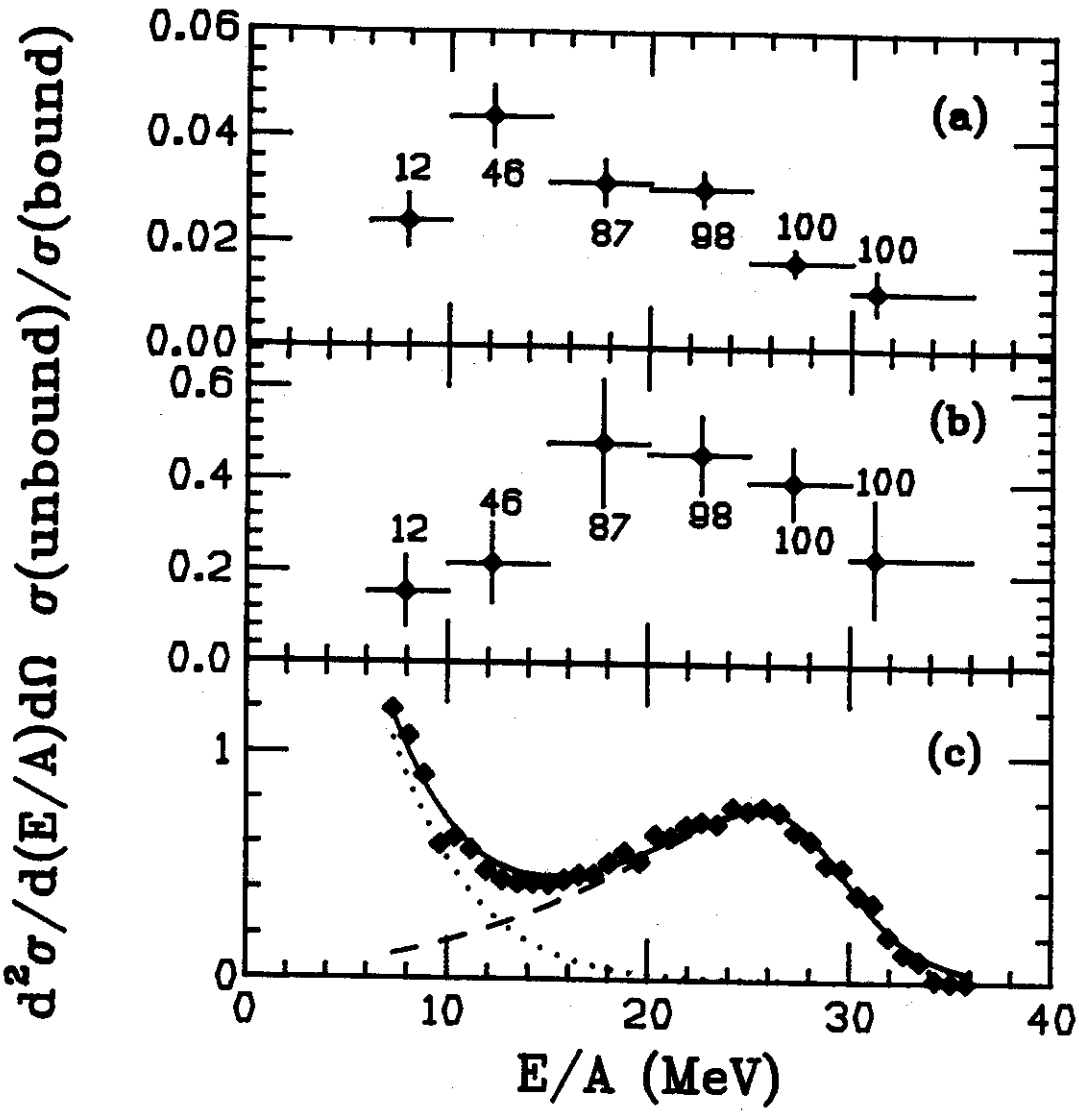

Fig. 11 - (a) and (b) show the population ratios of neutron-unbound states in ^{13}C to the ^{13}C bound states as a function of ^{12}C kinetic energy at 15°. In (a) the unbound state is at 9.50 MeV, and in (b) there are three unresolved unbound states at 7.49-MeV, 7.55-MeV, and 7.69-MeV. The numbers in (a) and (b) indicate the percentage of QE ^{13}C in the bound-state yield for the corresponding energy bin. (c) shows the ^{13}C singles spectrum at 15°. The solid, dotted, and dashed lines are from a fit described in the text.

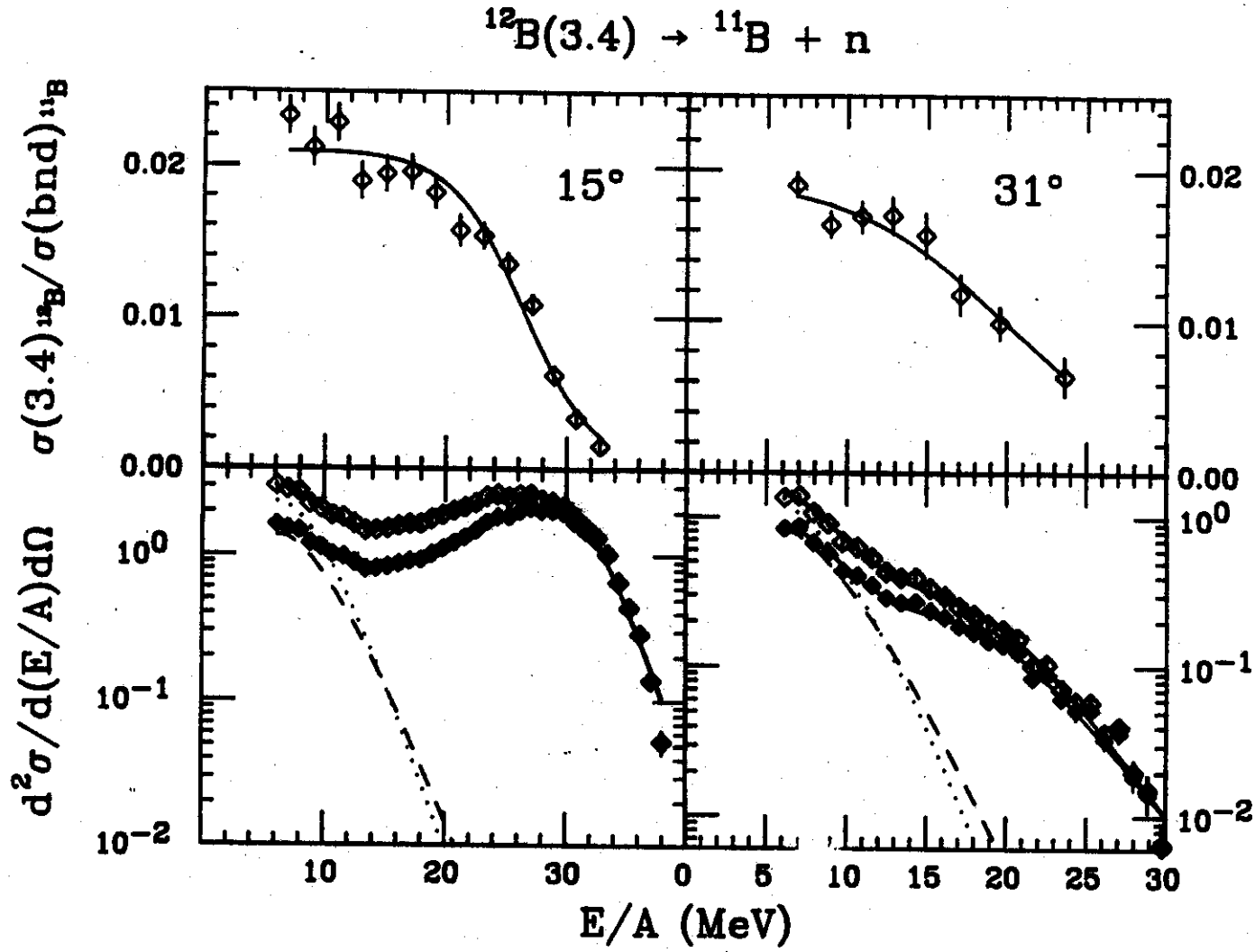

Fig. 12 - The upper plots show the ratio of the population of the 3.388-MeV state in ^{12}B to the bound-state population of ^{11}B as a function of ^{11}B kinetic energy. The solid lines are a fit to the data. The open symbols in the lower plots show the singles cross section of ^{11}B at 15° and 31° before correcting for feeding, and the closed symbols show the cross sections after the correction. The solid, dashed, and dotted lines in the lower plots come from a fit described in the text.